Lubricated axisymmetric gravity currents of power-law fluids

Ayala A. Gyllenberg[1] and Roiy Sayag[1,2,3],†

[1]Department of Mechanical Engineering, Ben-Gurion University of the Negev, Beer-Sheva 8410501, Israel

[2]Department of Environmental Physics, BIDR, Ben-Gurion University of the Negev, Sde Boker 8499000, Israel

[3]Department of Physics, Ben-Gurion University of the Negev, Beer-Sheva 8410501, Israel

The motion of glaciers over their bedrock or drops of fluid along a solid surface can become unstable when these substrates are lubricated. Previous studies modelled such systems as coupled gravity currents (GCs), consisting of one fluid that lubricates the flow of another fluid, and having two propagating fronts. When both fluids are Newtonian and discharged at constant flux, global similarity solutions were found. However, when the top fluid is strain-rate softening, experiments have shown that each fluid front evolved with a different exponent. Here, we explore theoretically and numerically such lubricated GCs consisting of axisymmetric spreading of a power-law fluid on top of a Newtonian fluid, where each fluid volume grows in time like t^α. We find that the structure imposed by the non-Newtonian flow precludes general self-similarity, unlike purely Newtonian GCs. Consequently, we identify outstripping solutions in which the inner fluid front outstrips the outer fluid front. Despite the absence of a general global similarity solution, we find similarity solutions in several asymptotic limits. These include the purely Newtonian limit for any α, the case of $\alpha = 5$ for a general power-law fluid, asymptotic limits in the viscosity ratio, and in the vicinity of the fluid fronts. Many of our theoretical predictions are found to be consistent with recent laboratory experiments. Discrepancies suggest the presence of hydrofracturing or wall slip near the fronts, and potentially, a progressive significance of extensional stresses as front outstripping is approached.

Key words: gravity currents, complex fluids, geophysical and geological flows, interfacial flows (free surface)

† Email address for correspondence: roiy@bgu.ac.il

1. Introduction

Gravity-driven flows of one fluid over another can involve complex interactions between the two fluids, which can lead to a rich dynamical behaviour. Such flows occur in a wide range of natural and human-made systems, as in lava flow over less viscous lava (Balmforth *et al.* 2000; Griffiths 2000), spreading of the lithosphere over the mid-mantle boundary (Lister & Kerr 1989; Dauck *et al.* 2019), ice flow over an ocean (Kivelson *et al.* 2000; DeConto & Pollard 2016) and over bedrock consisting of sediments and water (Fowler 1987; Stokes *et al.* 2007), flows in permeable rocks (Woods & Mason 2000), liquid drops deforming over lubricated surfaces (Daniel *et al.* 2017), and droplets motion on liquid-infused surfaces (Keiser *et al.* 2017).

The flow of gravity currents (GCs) in circular geometry has been studied with a range of boundary conditions. In the absence of a lubricating layer, a common boundary condition along the base of a sole GC is no-slip. Such GCs of Newtonian fluids that are discharged at a rate proportional to t^α, where t is time and α is a non-negative scalar, admit similarity solutions in which the front evolves proportionally to $t^{(3\alpha+1)/8}$ (Huppert 1982). Similar axisymmetric GCs of power-law fluids having exponent n, where $n = 1$ represents a Newtonian fluid and $n > 1$ represents a strain-rate softening fluid, also admit similarity solutions in which the front propagation is proportional to $t^{[\alpha(2n+1)+1]/(5n+3)}$ (Sayag & Worster 2013).

On the other extreme, the presence of a lower fluid layer can significantly reduce friction at the base of the top fluid, resulting in extensionally dominated GCs. This is the case, for example, for ice shelves, which deform over the relatively inviscid oceans with weak friction along their interface. The late-time front evolution of such axisymmetric GCs of Newtonian fluids is proportional to t and is believed to be stable (Pegler & Worster 2012). However, when the top fluid is strain-rate softening, an initially axisymmetric front can become unstable and develop fingering patterns consisting of tongues separated by rifts (Sayag & Worster 2019).

In the more general case, friction along the base of GCs can vary spatiotemporally, as their stress field evolves. For example, the interface of an ice sheet with its underlying bedrock can consist of distributed melt water and sediments (e.g. Vogel *et al.* 2005). Subglacial sediments are believed to deform viscoplastically (Iverson, Hooyer & Baker 1998; Tulaczyk, Kamb & Engelhardt 2000; Kamb 2001; Joughin, MacAyeal & Tulaczyk 2004; Schoof 2004), and when saturated with water, the ice basal friction may be affected significantly by a complex subglacial hydrological network that can evolve in time (e.g. Nanni *et al.* 2021). Consequently, subglacial lubrication can collectively impose non-uniform and time-dependent friction along the ice base, and evolve spatiotemporally under the stresses imposed by the ice layer (Fowler 1981; Schoof & Hewitt 2013). This coupled ice–subglacial-water system may become unstable either over hard beds (Walder 1982; Creyts & Schoof 2009) or over sediment beds (Kyrke-Smith & Fowler 2014; Kasmalkar, Mantelli & Suckale 2019), and may contribute to the formation of complex flow patterns, such as ice streams and ice surges (Fowler 1987; Fowler & Johnson 1995; Stokes *et al.* 2007; Sayag & Tziperman 2009; Kyrke-Smith, Katz & Fowler 2013). Such lubricated flows with spatiotemporally evolving friction were also modelled as two coupled GCs of Newtonian fluids spreading axisymmetrically one on top of the other (Kowal & Worster 2015). The early stage of these flows follows a similarity solution, in which the fronts of the two fluids evolve like $t^{1/2}$, as in non-lubricated (no-slip) GCs (Huppert 1982), but they can have a radially non-monotonic thickness. Furthermore, laboratory experiments were found to be consistent with the similarity solutions after an initial transient state, but became unstable at a later stage, developing fingering patterns (Kowal
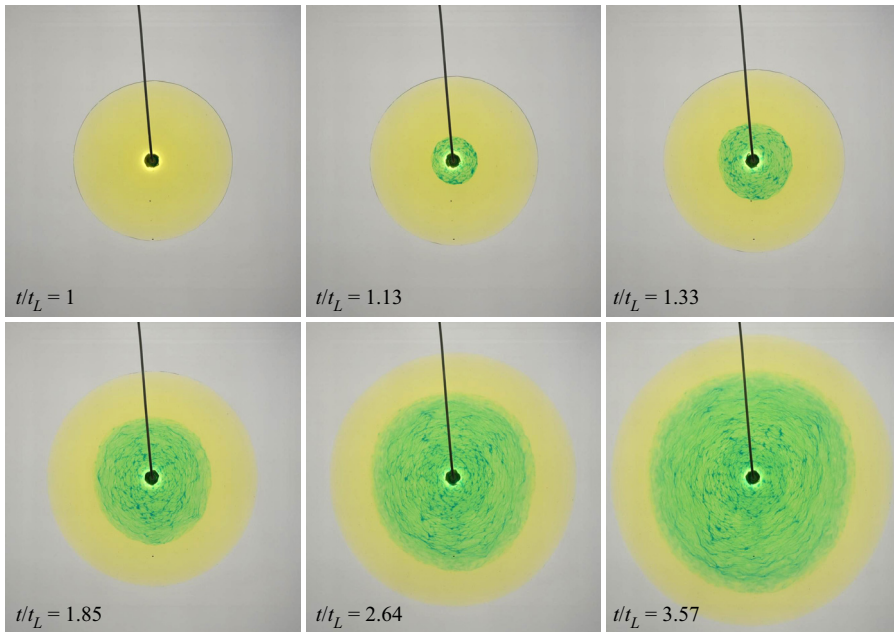
Figure 1. Snapshots from a laboratory experiment (Kumar *et al.* 2021) of a lubricated GC that consists of a strain-rate softening fluid (yellow) lubricated by a sugar solution (blue, appears green). The marked time at each snapshot is relative to the discharge initiation time t_L of the lubricating fluid.

& Worster 2015). It has been suggested that such instabilities appear when the jump in hydrostatic pressure gradient across the lubrication front is negative (Kowal & Worster 2019*a*,*b*).

Despite the wide range of natural lubricated GCs that involve non-Newtonian fluids, the radial flow of a non-Newtonian fluid over a lubricated layer of Newtonian fluid has just recently been explored experimentally (Kumar *et al.* 2021). Motivated by glacier flow over lubricated bedrock, the experimental set-up consisted of a GC of a strain-rate softening fluid (xanthan gum solution) that has a power-law viscous deformation similar to ice (Glen 1952), and a lubricating GC of a less viscous Newtonian fluid (diluted sugar solution). The pattern of both fluids in those constant flux ($\alpha = 1$) experiments remained axisymmetric throughout the flow (figure 1), in contrast to the fingering patterns that emerged in the purely Newtonian experiments (Kowal & Worster 2015), as long as the flux ratio of the lubricating fluid to the non-Newtonian fluid was lower than ~ 0.06. The fronts of the two fluids appeared to have a power-law time evolution with different exponents. In particular, the front of the top non-Newtonian fluid evolved with the same exponent $(2n + 2)/(5n + 3)$ as a non-lubricated power-law fluid (Sayag & Worster 2013), whereas the front of the Newtonian lubricating fluid evolved with an exponent $1/2$, similar to a Newtonian non-lubricated GC (Huppert 1982). Despite the similarity of the exponents with non-lubricated GCs, the fronts of those lubricated GCs evolved faster due to larger intercepts. In addition, in contrast with the monotonically declining thickness of non-lubricated GCs, the thickness of the lubricated, non-Newtonian fluid was found to be nearly uniform in the lubricated part of the flow, while that of the lubricating fluid was non-monotonic with localized spikes.

Following up the experimental study of Kumar *et al.* (2021), here we develop a theory for lubricated axisymmetric GCs of power-law fluids, and explore its major consequences.
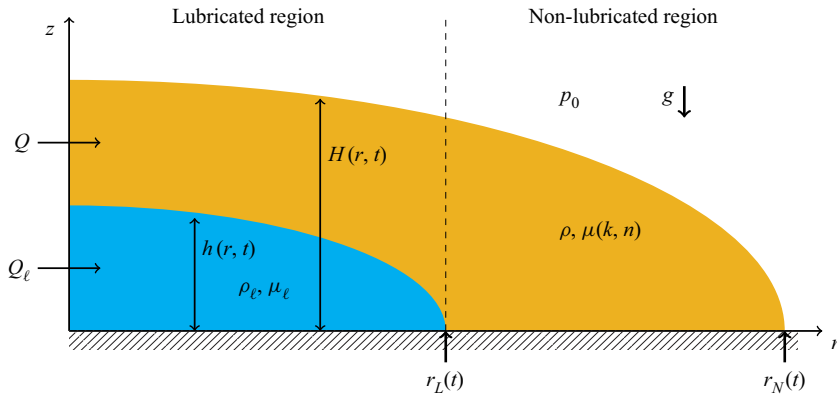
Figure 2. Diagram illustrating a GC of Newtonian fluid (blue) lubricating a GC of a power-law fluid (yellow). Exact solutions are singular at the origin, apart from the illustrated constant volume case $\alpha = 0$.

Specifically, we develop a mathematical model for axisymmetric flow of a viscous GC of a power-law fluid lubricated by a Newtonian GC, considering a general input flux of the form t^{α}, and show that in the general case, the flow has no global similarity solution of the first kind (§ 2). We then describe the numerical solver (§ 3), investigate several special cases that have similarity solutions (§ 4), and explore the possibility that the inner lubricating front outstrip the outer front (§ 5). Finally, we investigate the case of constant flux discharge (§ 6), compare our theoretical predictions with the laboratory experiments of Kumar *et al.* (2021) (§ 7), and discuss caveats and implications (§ 8).

2. Mathematical model

Consider a power-law fluid having viscosity μ and density ρ that spreads axisymmetrically under its own weight over a horizontal rigid surface. Simultaneously, a lubricating film of Newtonian immiscible fluid of viscosity μ_ℓ and density ρ_ℓ spreads axisymmetrically over the substrate and below the power-law fluid (figure 2). Both fluids are discharged at the origin of a cylindrical coordinate system in which r is the radial coordinate and z is the vertical coordinate. The upper and lower fluid fronts are denoted by $r_N(t)$ and $r_L(t)$ respectively, and the corresponding fluid thicknesses are denoted by $H(r, t) - h(r, t)$ and $h(r, t)$, respectively, where t is the time variable. Beginning the discharge of the lubricating fluid at a time delay t_L, with respect to the upper fluid, creates two regions in the flow: an inner, lubricated region ($r \leqslant r_L$) in which the power-law fluid flows at a finite velocity along the interface with the lubricating fluid, and an outer, non-lubricated region ($r_L < r \leqslant r_N$) in which the power-law fluid meets the substrate and has zero velocity along it.

We assume that the radial extent of the flow is much greater than its thickness in both fluid layers, and that the flow is primarily radial. Together with the no-slip boundary condition along the substrate, this implies that the flow is shear-dominated in the non-lubricated region and in the lower fluid layer in the lubricated region. We also assume that the flow in the upper fluid layer in the lubricated region is shear-dominated due to back pressure applied by the non-lubricated layer downstream, which inhibits the growth of extensional stresses. We elaborate further on this assumption in § 8. Consequently, we apply the lubrication approximation in each fluid layer i, with a dominant strain rate $\partial u_i / \partial z$, where $u_i(r, z, t)$ is the radial velocity component. Therefore, the axisymmetric Cauchy equations for each fluid layer, simplified for flows of low Reynolds numbers and

lubrication approximations, are

$$\frac{\partial p_i}{\partial r} = \frac{\partial}{\partial z}\left(\mu_i \frac{\partial u_i}{\partial z}\right), \tag{2.1a}$$

$$\frac{\partial p_i}{\partial z} = -\rho_i g, \tag{2.1b}$$

$$\frac{1}{r}\frac{\partial(r u_i)}{\partial r} + \frac{\partial w_i}{\partial z} = 0, \tag{2.1c}$$

to leading order, where w_i is the vertical velocity component, p_i is the pressure field, and g is the gravitational acceleration. The pressure is determined hydrostatically in (2.1b) because we assume a large Bond number, implying that the effects of surface tension are negligible compared to gravity. Since (2.1) satisfy the lubrication approximation, this model does not describe accurately the problem at early times, before the fluid radial extent is sufficiently greater than its thickness. We estimate the instant when lubrication approximation is first satisfied in § 7, where we compare the theoretical predictions with the experimental data.

The viscosity of the power-law fluid is determined by

$$\mu = k\left(\tfrac{1}{2}\boldsymbol{E} : \boldsymbol{E}\right)^{1/2(1/n-1)}, \tag{2.2}$$

where $\boldsymbol{E}$ is the strain-rate tensor, k is the consistency coefficient, and n is the power-law exponent, which determines the fluid's response to stress. Specifically, $n = 1$ represents a Newtonian fluid with dynamical viscosity k, with $n > 1$ a shear-thinning fluid, and $n < 1$ a shear-thickening fluid. In the lubrication limit, $\boldsymbol{E} : \boldsymbol{E} \approx (\partial u/\partial z)^2$ to leading order, so the viscosity of the power-law fluid simplifies to

$$\mu = k\left|\frac{1}{2}\frac{\partial u}{\partial z}\right|^{1/n-1}. \tag{2.3}$$

We assume that the total volumes of the power-law fluid and the Newtonian fluid evolve following a power law in time given by

$$2\pi \int_0^{r_N} (H - h) r \, \mathrm{d}r = Q t^\alpha, \tag{2.4a}$$

and for $t > t_L$,

$$2\pi \int_0^{r_L} h r \, \mathrm{d}r = Q_\ell \left(t - t_L\right)^\alpha, \tag{2.4b}$$

where α is a constant exponent, and Q and Q_ℓ are constant coefficients representing, for instance, the discharge flux of each fluid when $\alpha = 1$.

2.1. *The non-lubricated region*

In the non-lubricated region, the power-law fluid meets the substrate, and the lubricating fluid is absent. Integrating (2.1b), the pressure distribution is

$$p(z, r, t) = p_0 + \rho g(H(r, t) - z), \tag{2.5}$$

where p_0 is the ambient pressure over the top free surface of the power-law fluid. Integration of the radial force balance (2.1a) across the depth of the fluid layer, together

with no-slip boundary conditions along the substrate and no stress along the free surface

$$u(z = 0) = 0, \quad \mu \frac{\partial u}{\partial z}(z = H) = 0, \qquad (2.6a,b)$$

gives the radial velocity field

$$u(z, r, t) = 2^{1-n} \left(\frac{\rho g}{k}\right)^n \frac{\partial H}{\partial r} \left|\frac{\partial H}{\partial r}\right|^{n-1} \frac{1}{1+n} \left[(H - z)^{n+1} - H^{n+1}\right]. \qquad (2.7)$$

Similar integration of the continuity equation (2.1c), accounting for a free surface at the upper boundary $z = H(r, t)$, and assuming no normal flow through the substrate, gives the Reynolds equation

$$\frac{\partial H}{\partial t} + \frac{1}{r} \frac{\partial (rq)}{\partial r} = 0, \qquad (2.8)$$

which should satisfy the boundary conditions

$$H(r = r_N) = 0 \quad \text{and} \quad q(r = r_N) = 0, \qquad (2.9a,b)$$

where the local flux q is determined using (2.7) to give

$$q = \int_0^H u \, dz = -2^{1-n} \left(\frac{\rho g}{k}\right)^n \frac{\partial H}{\partial r} \left|\frac{\partial H}{\partial r}\right|^{n-1} \frac{1}{n+2} H^{n+2}. \qquad (2.10)$$

2.2. *The lubricated region*

As in the non-lubricated region and assuming continuity of pressure at the fluid–fluid interface $z = h$, the pressure in the lubricated region is determined hydrostatically by

$$p(z) = p_0 + \rho g(H - z), \quad \text{where } h \leqslant z \leqslant H, \qquad (2.11a)$$

$$p_\ell(z) = p_0 + \rho g(H - h) + \rho_\ell g(h - z), \quad \text{where } 0 \leqslant z \leqslant h. \qquad (2.11b)$$

The radial force balances simplify to

$$\frac{k}{2^{1/n-1}} \frac{\partial}{\partial z} \left(\frac{\partial u}{\partial z} \left|\frac{\partial u}{\partial z}\right|^{1/n-1}\right) = \frac{\partial p}{\partial r}, \quad \text{where } h \leqslant z \leqslant H, \qquad (2.12a)$$

$$\mu_\ell \frac{\partial^2 u_\ell}{\partial z^2} = \frac{\partial p_\ell}{\partial r}, \quad \text{where } 0 \leqslant z \leqslant h, \qquad (2.12b)$$

together with the boundary conditions

$$u_\ell = 0, \quad \text{where } z = 0, \qquad (2.13a)$$

$$u_\ell = u, \quad k \left|\frac{1}{2} \frac{\partial u}{\partial z}\right|^{1/n-1} \frac{\partial u}{\partial z} = \mu_\ell \frac{\partial u_\ell}{\partial z}, \quad \text{where } z = h, \qquad (2.13b)$$

$$\frac{\partial u}{\partial z} = 0, \quad \text{where } z = H, \qquad (2.13c)$$

which represent, respectively, no-slip along the solid substrate, continuous flow velocity and shear stress at the fluid–fluid interface, and no shear stress along the free surface of the power-law fluid. Integrating the radial force balance (2.12) across the thickness of each

949 A40-6

fluid layer, and using the boundary conditions (2.13), we get the radial velocity fields in each fluid layer:

$$u(z, r, t) = 2^{1-n} \left(\frac{\rho g}{k} \right)^n \frac{1}{1+n} \frac{\partial H}{\partial r} \left| \frac{\partial H}{\partial r} \right|^{n-1} \left[(H - z)^{1+n} - (H - h)^{1+n} \right]$$

$$- \frac{\rho g}{\mu_\ell} \left[\frac{\partial H}{\partial r} \left(Hh - \frac{h^2}{2} \right) + \frac{h^2}{2} \frac{\rho_\ell - \rho}{\rho} \frac{\partial h}{\partial r} \right], \quad (2.14a)$$

$$u_\ell(z, r, t) = -\frac{\rho g}{\mu_\ell} \left[\frac{\partial H}{\partial r} \left(Hz - \frac{z^2}{2} \right) + \frac{1}{2} \frac{\rho_\ell - \rho}{\rho} \frac{\partial h}{\partial r} \left(2hz - z^2 \right) \right]. \quad (2.14b)$$

The Reynolds equations corresponding to each fluid layer have forms similar to those of the non-lubricated region,

$$\frac{\partial h}{\partial t} + \frac{1}{r} \frac{\partial (r q_\ell)}{\partial r} = 0, \quad (2.15a)$$

$$\frac{\partial (H - h)}{\partial t} + \frac{1}{r} \frac{\partial (r q)}{\partial r} = 0, \quad (2.15b)$$

and should satisfy the boundary conditions

$$h = 0, \quad q_\ell = 0 \quad \text{at } r = r_L, \quad (2.16a)$$

and

$$q^+ = q^-, \quad H^+ = H^- \quad \text{at } r = r_L, \quad (2.16b)$$

where (2.16b) signifies flux and height continuity across r_L. The local fluxes result from integrating (2.14) to get

$$q = \int_h^H u \, \mathrm{d}z = -2^{1-n} \left(\frac{\rho g}{k} \right)^n \frac{\partial H}{\partial r} \left| \frac{\partial H}{\partial r} \right|^{n-1} \frac{1}{n+2} (H - h)^{n+2}$$

$$- (H - h) \frac{h \rho g}{\mu_\ell} \left[\frac{\partial H}{\partial r} (H - h) + \frac{h}{2} \left(\frac{\partial H}{\partial r} + \frac{\rho_\ell - \rho}{\rho} \frac{\partial h}{\partial r} \right) \right], \quad (2.17a)$$

$$q_\ell = \int_0^h u_\ell \, \mathrm{d}z = -\frac{h^2}{2} \frac{\rho g}{\mu_\ell} \left[\frac{\partial H}{\partial r} (H - h) + \frac{2h}{3} \left(\frac{\partial H}{\partial r} + \frac{\rho_\ell - \rho}{\rho} \frac{\partial h}{\partial r} \right) \right]. \quad (2.17b)$$

We note that without a lubricant, this set of partial differential equations (PDEs) is reduced to that of the non-lubricated region, which is consistent with the non-lubricated power-law GC model (Sayag & Worster 2013), and particularly with the Newtonian non-lubricated GC when $n = 1$ (Huppert 1982). In addition, the full PDE set for the Newtonian case ($n = 1$) and constant source fluxes ($\alpha = 1$) is consistent with the model for Newtonian lubricated GCs (Kowal & Worster 2015).

2.3. *Dimensionless equations*

We non-dimensionalize equations (2.4), (2.8)–(2.10) and (2.15)–(2.17) with the following time, length and height scales:

$$t \equiv \mathcal{T}\hat{t}, \tag{2.18a}$$

$$r \equiv \left(\left(\frac{\rho g}{k}\right)^n Q^{2n+1} \mathcal{T}^{\alpha(1+2n)+1}\right)^{1/(5n+3)} \hat{r}, \tag{2.18b}$$

$$(H, h) \equiv \left(\left(\frac{\rho g}{k}\right)^{-2n} Q^{1+n} \mathcal{T}^{\alpha(1+n)-2}\right)^{1/(5n+3)} (\hat{H}, \hat{h}), \tag{2.18c}$$

where hats denote dimensionless quantities. The resulting dimensionless model, dropping hats, in the non-lubricated region $r_L \leqslant r \leqslant r_N$ is

$$\frac{\partial H}{\partial t} + \frac{1}{r}\frac{\partial(rq)}{\partial r} = 0, \tag{2.19}$$

where

$$q = -\mathcal{N}\frac{\partial H}{\partial r}\left|\frac{\partial H}{\partial r}\right|^{n-1} H^{n+2}, \quad \mathcal{N} = \frac{2^{1-n}}{n+2}, \tag{2.20a,b}$$

and in the lubricated region $0 \leqslant r \leqslant r_L$ it is

$$\frac{\partial h}{\partial t} + \frac{1}{r}\frac{\partial(rq_\ell)}{\partial r} = 0, \tag{2.21a}$$

$$\frac{\partial(H-h)}{\partial t} + \frac{1}{r}\frac{\partial(rq)}{\partial r} = 0, \tag{2.21b}$$

where

$$q = -\mathcal{N}\frac{\partial H}{\partial r}\left|\frac{\partial H}{\partial r}\right|^{n-1}(H-h)^{2+n}$$

$$- \mathcal{M}h(H-h)\left[\frac{\partial H}{\partial r}(H-h) + \left(\frac{\partial H}{\partial r} + \mathcal{D}\frac{\partial h}{\partial r}\right)\frac{h}{2}\right], \tag{2.22a}$$

$$q_\ell = -\mathcal{M}\frac{h^2}{2}\left[\frac{\partial H}{\partial r}(H-h) + \frac{2h}{3}\left(\frac{\partial H}{\partial r} + \mathcal{D}\frac{\partial h}{\partial r}\right)\right], \tag{2.22b}$$

and where the boundary conditions are

$$q = 0, \quad H = 0 \quad \text{at } r = r_N, \tag{2.23a}$$

$$q_\ell = 0, \quad h = 0, \quad q^+ = q^-, \quad H^+ = H^- \quad \text{at } r = r_L, \tag{2.23b}$$

$$\lim_{r\to 0}(2\pi rq) = \alpha t^{\alpha-1}, \quad \text{and for } t > t_L \quad \lim_{r\to 0}(2\pi rq_\ell) = \alpha\mathcal{Q}(t-t_L)^{\alpha-1}, \tag{2.23c}$$

and the total instantaneous volumes of the power-law and Newtonian fluids are

$$2\pi\int_0^{r_N}(H-h)r\,\mathrm{d}r = t^\alpha, \tag{2.24a}$$

and for $t > t_L$

$$2\pi\int_0^{r_L}hr\,\mathrm{d}r = (t-t_L)^\alpha, \tag{2.24b}$$

respectively. The resulting dimensionless quantities

$$\left.\begin{array}{c} \mathscr{Q} \equiv \dfrac{Q_\ell}{Q}, \quad \mathscr{D} \equiv \dfrac{\rho_\ell - \rho}{\rho}, \quad n, \quad \alpha, \\[4mm] \mathscr{M} \equiv \dfrac{\mu}{\mu_\ell} = \dfrac{\rho g}{\mu_\ell} \left(\dfrac{k}{\rho g}\right)^{8n/(5n+3)} \left(\dfrac{\mathcal{T}^{5-\alpha}}{Q}\right)^{(n-1)/(5n+3)}, \end{array}\right\} \tag{2.25a–e}$$

represent respectively the discharge flux ratio, the relative density difference of the lubricating and power-law fluids, the power-law fluid exponent, the volume growth exponent, and the dynamic viscosity ratio.

The scale for the non-Newtonian fluid viscosity is based on the leading-order viscosity (2.3) and the spatial scales in (2.18). Specifically, we evaluate the characteristic scale for the strain rate $\partial u/\partial z$ in (2.3) using (2.7) to get $[\partial u/\partial z] \propto (\rho g/k)^n H^{2n}/R^n$. Substituting the scales (2.18b,c) in the strain rate, we find that the characteristic viscosity scale is $[\mu] \sim \rho g (k/\rho g)^{8n/(5n+3)} (\mathcal{T}^{5-\alpha}/Q)^{(n-1)/(5n+3)}$, which depends on the time scale $\mathcal{T}$. That time scale, which also enters the viscosity ratio $\mathscr{M}$ (see (2.25e)), is scaled out of the equations in the two special cases $n = 1$ and $\alpha = 5$. Therefore, in the late-time limit ($t/t_L \gg 1$), the system no longer depends on the time scale t_L, and admits a global similarity solution of the first kind in these two special cases. For any other values of n and α, including the constant flux case ($\alpha = 1$), such global similarity solutions do not exist. Nevertheless, as we show in § 4, we find several additional asymptotic limits in which part of the flow evolves in a self-similar manner.

In the general case $n \neq 1$ and $\alpha \neq 5$, there are enough relations to determine the time scale $\mathcal{T}$ (see (2.18)) independently of the height and radial scales. Specifically, requiring that the scales of the two contributions to the flux in the top fluid layer (2.22a) balance leads to the relation $\mathscr{M}(\mathcal{T}) = \mathscr{N}$ that can be solved for the time scale $\mathcal{T}$, which upon substitution in (2.18) leads to independent radial scale $\mathcal{R}$ and thickness scale $\mathcal{H}$, given by

$$\mathcal{T}^{(1-n)(\alpha-5)} = Q^{n-1} \left(\mathscr{N} \frac{\mu_\ell}{\rho g}\right)^{5n+3} \left(\frac{\rho g}{k}\right)^{8n}, \tag{2.26a}$$

$$\mathcal{R}^{(1-n)(\alpha-5)} = Q^{2(n-1)} \left(\mathscr{N} \frac{\mu_\ell}{\rho g}\right)^{\alpha+1+2\alpha n} \left(\frac{\rho g}{k}\right)^{n(3\alpha+1)}, \tag{2.26b}$$

$$\mathcal{H}^{(1-n)(\alpha-5)} = Q^{n-1} \left(\mathscr{N} \frac{\mu_\ell}{\rho g}\right)^{\alpha-2+\alpha n} \left(\frac{\rho g}{k}\right)^{2n(\alpha-1)}. \tag{2.26c}$$

Therefore, in the more general case ($n \neq 1$ and $\alpha \neq 5$), which does not admit global similarity solution of the first kind, the above may represent the time, radius and thickness scales. The time scale $\mathcal{T}$ can also be set by the lubricating fluid discharge time t_L, as we do when comparing the theoretical predictions to the experimental measurements in § 7.

3. Numerical solutions

We solve the dimensionless model (2.19)–(2.25a–e) numerically explicitly using the Matlab PDEPE solver, with an open-ended, non-uniform and time-dependent adaptive spatial mesh, and using the dimensional t_L as the time scale $\mathcal{T}$, so that $\hat{t}_L = 1$. We find that lower spatial resolution can be used in most of the domain if the mesh is spaced logarithmically, and is denser around the fluid fronts, where the fluid heights drop sharply
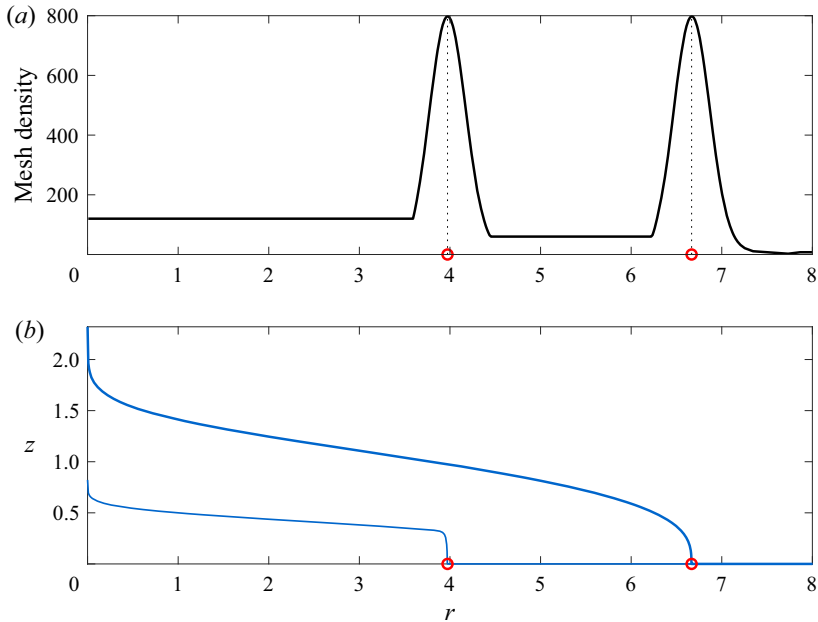
Figure 3. (*a*) Mesh density and (*b*) a solution at time $t/t_L = 100$, showing the lubricated fluid (thick) and the lubricating fluid (thin) for $n = 1$, $\alpha = 1$, $\mathscr{M} = 1$, $\mathscr{Q} = 0.2$ and $\mathscr{D} = 0.1$. Front positions (red circles) are determined where each fluid thickness drops below 10^{-6}. Substrate is not pre-wetted ahead of the intrusion, and each fluid thickness ahead of its front diminishes rapidly to zero.

and the slopes $\partial H/\partial r$ and $\partial h/\partial r$ become singular. Therefore, we use a non-uniform spatial mesh that consists of two Gaussian distributions centred at the fronts r_N and r_L, and uniform distributions between the origin and r_L, the two fronts, and beyond r_N (figure 3). The instantaneous front positions $r_N(t)$ and $r_L(t)$ are determined where $H(r, t) \leqslant 10^{-6}$ and $h(r, t) \leqslant 10^{-6}$, respectively. Since the fronts evolve, we divide the simulation time into a set of intervals, and over each interval, we solve the PDE system and then adapt the spatial mesh. The mesh adaptation is done by predicting the front positions in the next time interval using the recent solution and the front evolution equations

$$\dot{r}_N(t) = \lim_{r \to r_N} \frac{q}{H} \quad \text{and} \quad \dot{r}_L(t) = \lim_{r \to r_L} \frac{q_\ell}{h}. \tag{3.1a,b}$$

This technique allows us to keep higher mesh density centred at the front positions, where variations in the fields are larger, and lower density elsewhere, where variations are milder.

We validated our numerical solver using several known asymptotic solutions. In the limit $\mathscr{Q} = 0$ (no lubricating fluid), our model converges to a GC that propagates under a no-slip condition along the substrate, which has a similarity solution $r_N(t) \propto t^{[\alpha(2n+1)+1]/(5n+3)}$ (Huppert 1982; Sayag & Worster 2013). We find that our numerical solutions for the fluid heights and for the leading front are consistent with those theoretical predictions (Appendix A). In particular, the discrepancy between the predicted and computed exponents is less than 5×10^{-3} and can be minimized further with a higher spatial resolution. In the limit $n = 1$ and $\alpha = 1$, our model converges to a purely Newtonian lubricated GC released at constant flux, which has a similarity solution $r_L, r_N \propto t^{1/2}$ (Kowal & Worster 2015). We find that our numerical solutions are consistent with both the front and thickness predictions for a wide range of $\mathscr{M}$ and $\mathscr{Q}$ values (Appendix A).

949 A40-10

4. Similarity solutions

The model described by (2.19)–(2.25) admits similarity solutions in several special cases. Specifically, global similarity solutions exist when the top fluid is also Newtonian ($n = 1$), or when the mass-discharge exponent is $\alpha = 5$. In addition, part of the flow evolves in a self-similar manner in the asymptotic limits of the viscosity ratio $\mathscr{M}$. Finally, for any parameter combination, the solutions in the vicinity of each front evolve in a self-similar manner.

4.1. *The similarity solution for Newtonian fluids ($n = 1$)*

When the top fluid is Newtonian ($n = 1$), the viscosity ratio $\mathscr{M}$ is independent of $\mathcal{T}$, and the resulting purely Newtonian coupled flow admits a global similarity solution. This case, restricted to a constant flux ($\alpha = 1$), has been explored thoroughly (Kowal & Worster 2015). For the general case of $\alpha \geqslant 0$, the PDE set can be reduced to an ordinary differential equation set with similarity variable

$$\eta = \frac{r}{t^{(3\alpha+1)/8}} \left(\frac{\rho g}{k} Q^3 \right)^{-1/8}, \tag{4.1}$$

and a solution of the form

$$(H, h) = t^{(\alpha-1)/4} \left(Q \frac{k}{\rho g} \right)^{1/4} (F, f), \tag{4.2a}$$

where F and f are dimensionless functions of η. Therefore, the fronts of both the lubricated and lubricating fluids evolve like

$$(r_N, r_L) = (\eta_N, \eta_L) \, t^{(3\alpha+1)/8} \left(Q^3 \frac{\rho g}{k} \right)^{1/8}, \tag{4.2b}$$

where $\eta_N \equiv \eta(r = r_N)$ and $\eta_L \equiv \eta(r = r_L)$ are numerical coefficients of order 1. These solutions have structure identical to that of the classical solution for Newtonian GCs (Huppert 1982). Upon substitution, the Reynolds equations (2.8) and (2.15) become, for the non-lubricated region ($\eta_L \leqslant \eta \leqslant \eta_N$),

$$\left(\frac{\alpha - 1}{4} \right) F - \left(\frac{3\alpha + 1}{8} \right) \eta F' = \frac{1}{3\eta} (\eta F' F^3)', \tag{4.3}$$

where prime denotes a derivative with respect to η, and for the lubricated region ($0 \leqslant \eta \leqslant \eta_L$),

$$\left(\frac{\alpha - 1}{4} \right) (F - f) - \left(\frac{3\alpha + 1}{8} \right) \eta \left(F' - f' \right) + \frac{1}{\eta} (\eta q)' = 0, \tag{4.4a}$$

$$\left(\frac{\alpha - 1}{4} \right) f - \left(\frac{3\alpha + 1}{8} \right) \eta f' + \frac{1}{\eta} (\eta q_\ell)' = 0, \tag{4.4b}$$

where

$$q = -\tfrac{1}{3} F'(F - f)^3 - \mathscr{M} f(F - f)[F'(F - f) + \tfrac{1}{2} f(\mathscr{D} f' + F')], \tag{4.5a}$$

$$q_\ell = -\mathscr{M} f^2 [\tfrac{1}{2} F'(F - f) + \tfrac{1}{3} f(\mathscr{D} f' + F')]. \tag{4.5b}$$
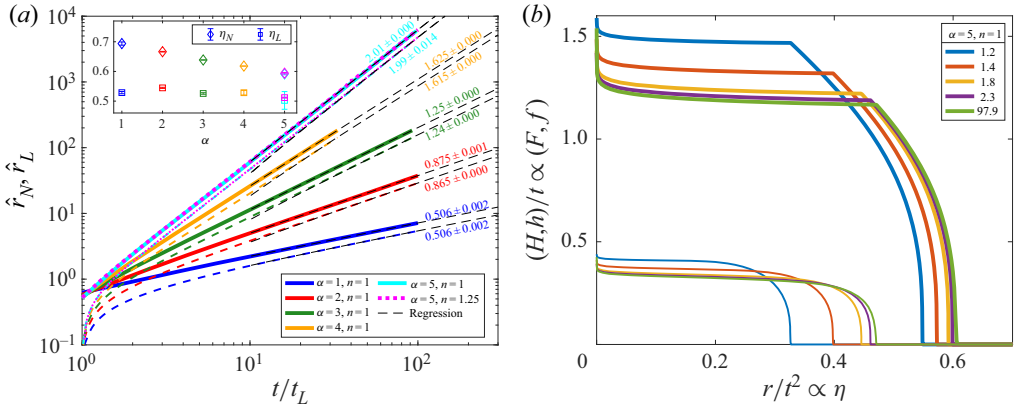
Figure 4. (*a*) The numerical solutions for the evolution of the dimensionless fronts for $\alpha = 1, 2, 3, 4, 5, n = 1$ and for $\alpha = 5, n = 1.25$ (coloured lines and dashed lines) for $\mathcal{Q} = 0.2$, $\mathcal{D} = 0.1$ and $\mathcal{M} = 100$. Regression to the late-time solutions ($t/t_L > 10$) to power-law evolution along one decade of time (dash, black) results in exponents (values in colour) consistent with the global similarity for the $n = 1$ cases ($t^{(3\alpha+1)/8}$, (4.2*b*)) and with the $\alpha = 5$ cases (t^2, (4.8*b*)). The inset shows the computed intercepts $\eta_N(\diamond)$, $\eta_L(\square)$ versus α. (*b*) The normalized thicknesses H/t, h/t along the normalized radius r/t^2 at selected dimensionless time t/t_L when $\alpha = 5$ and $n = 1$. This shows the relatively rapid convergence of the numerical solution to an asymptotic similarity solution (4.8), where the front positions at the late-time instant $t/t_L = 97.9$ are $\eta_N \approx 0.621$, $\eta_L \approx 0.473$, correspondingly with the computed values in the inset of (*a*).

The corresponding boundary conditions (2.23) become

$$F = 0, \quad q = 0 \quad \text{at } \eta = \eta_N, \tag{4.6a}$$

$$f = 0, \quad q_\ell = 0, \quad F^+ = F^-, \quad q^+ = q^- \quad \text{at } \eta = \eta_L, \tag{4.6b}$$

$$\lim_{\eta \to 0} 2\pi\eta q = \alpha, \quad \lim_{\eta \to 0} 2\pi\eta q_\ell = \alpha\mathcal{Q}, \tag{4.6c}$$

where the last condition implies convergence to a similarity solution a long time after the initiation of the fluid discharge, $t \gg t_L$.

For $\alpha = 1$, the model converges to that of Kowal & Worster (2015), and the similarity solutions that we predict for general α are consistent with our full numerical solution (figures 4 and 5).

4.2. *The similarity solution for mass-discharge exponent $\alpha = 5$*

When the top fluid is non-Newtonian, $n \neq 1$, the viscosity ratio $\mathcal{M}$ becomes independent of the time scale $\mathcal{T}$ for a discharge exponent $\alpha = 5$, and the resulting flow also admits a similarity solution with similarity variable

$$\eta = \frac{r}{t^2} \left[Q^{2n+1} \left(\frac{\rho g}{k} \right)^n \right]^{-1/(5n+3)}, \tag{4.7}$$

and a solution of the form

$$(H, h) = t \left[Q^{1+n} \left(\frac{k}{\rho g} \right)^{2n} \right]^{1/(5n+3)} (F, f), \tag{4.8a}$$
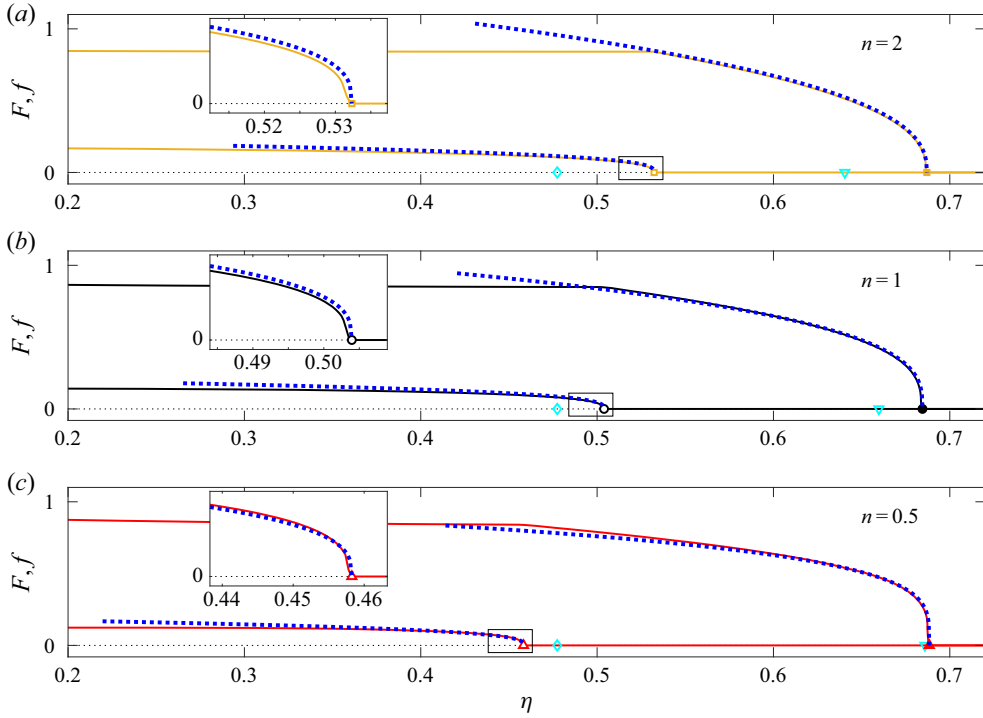
Figure 5. The asymptotic solutions in the vicinity of the fronts $F(\eta), f(\eta)$ (see (4.18a,b), (4.21)) given by the non-lubricated GC similarity solutions (blue dotted lines), compared with the full numerical solutions of lubricated GCs (solid lines) for $\mathcal{M} = 100$, $\mathcal{Q} = 0.1$, $\mathcal{D} = 1$, $\alpha = 1$ and $n = 0.5, 1, 2$ at $t/t_L \approx 20$. The positions of the fronts predicted by the non-lubricated GC solutions are cyan $\triangledown$ (η_N) and cyan $\lozenge$ (η_L), but to have the shapes of the two solutions more clearly compared, we translated the asymptotic solutions so that their fronts coincide with those of the lubricated GC solution ($\square$, $\circ$, $\triangle$ markers). Each inset zooms into the region near the lubricating fluid front marked by a rectangle.

where F and f are dimensionless functions of η. Therefore, the fronts of both the lubricated and lubricating fluids evolve like

$$(r_N, r_L) = (\eta_N, \eta_L) \, t^2 \left[Q^{2n+1} \left(\frac{\rho g}{k} \right)^n \right]^{1/(5n+3)}, \qquad (4.8b)$$

where η_N and η_L are numerical coefficients of order 1. Upon substitution, the Reynolds equations (2.8) and (2.15) become, for the non-lubricated region ($\eta_L \leqslant \eta \leqslant \eta_N$)

$$F - 2F'\eta = \mathcal{N} \, \frac{1}{\eta} (\eta F' \left| F' \right|^{n-1} F^{n+2})', \qquad (4.9)$$

and for the lubricated region ($0 \leqslant \eta \leqslant \eta_L$)

$$(F - f) - 2(F' - f')\eta + \frac{1}{\eta} (\eta q)' = 0, \qquad (4.10a)$$

$$f - 2f'\eta + \frac{1}{\eta} (\eta q_\ell)' = 0, \qquad (4.10b)$$

949 A40-13

where

$$q = -\mathcal{N} F' \left| F' \right|^{n-1} (F - f)^{n+2} - \mathcal{M} f (F - f) \left[F'(F - f) + \tfrac{1}{2} f (\mathcal{D} f' + F') \right], \quad (4.11a)$$

$$q_\ell = -\mathcal{M} f^2 \left[\tfrac{1}{2} F'(F - f) + \tfrac{1}{3} f (F' + \mathcal{D} f') \right]. \quad (4.11b)$$

The corresponding boundary conditions (2.23) become

$$F = 0, \quad q = 0 \quad \text{at } \eta = \eta_N, \quad (4.12a)$$

$$f = 0, \quad q_\ell = 0, \quad F^+ = F^-, \quad q^+ = q^- \quad \text{at } \eta = \eta_L, \quad (4.12b)$$

$$\lim_{\eta \to 0} 2\pi \eta q = 5, \quad \lim_{\eta \to 0} 2\pi \eta q_\ell = 5\mathcal{Q}. \quad (4.12c)$$

Figure 4 shows the numerical solution of the full PDE set for $\alpha = 5$ for varying power-law exponent values. We find that the numerical solutions are consistent with the predicted similarity solution (4.8). This consistency validates further the numerical simulation for the combination of lubricated GCs with lubricated power-law fluid.

We note that a similarity solution at $\alpha = 5$ arises also in other GCs with radial symmetry, but of different settings. We elaborate on this aspect in § 8.

4.3. *Similarity solutions for the asymptotic limits in $\mathcal{M}$: the upper fluid solid and liquid limits*

In the general case of $\alpha \neq 5$ and $n \neq 1$, our model does not admit global similarity solutions of the first kind. However, a similarity solution arises in part of the flow domain in each of the asymptotic limits of the viscosity ratio, in which the upper fluid layer is either relatively more viscous ($\mathcal{M} \gg 1$, the 'solid' limit) or relatively less viscous ($\mathcal{M} \ll 1$, the 'liquid' limit) compared with the lower fluid layer.

4.3.1. *The top layer solid limit, $\mathcal{M} \gg 1$*
The limit $\mathcal{M} \gg 1$ represents the case where the top fluid is much more viscous than the lubricating fluid. One motivation to study this limit is the geophysical setting of ice sheets creeping over less viscous lubricated beds. In this case, the leading-order scaling of the power-law fluid local flux in the lubricated region (2.22a) is

$$q \approx -\mathcal{M} h (H - h) \left[\frac{\partial H}{\partial r} (H - h) + \left(\frac{\partial H}{\partial r} + \mathcal{D} \frac{\partial h}{\partial r} \right) \frac{h}{2} \right], \quad (4.13)$$

which is identical to the scaling of the Newtonian lubricating fluid flux (2.22b). In such a case, the three scales $\mathcal{H}$, $\mathcal{R}$ and $\mathcal{T}$ in the lubricated region cannot be determined independently despite the fact that the upper fluid is a power-law fluid. Therefore, both fluids in the lubricated region have a similarity solution in which the dimensionless front in the lubricated region evolves with an n-independent exponent

$$r_L = \eta_L t^{(3\alpha+1)/8}, \quad (4.14)$$

where the intercept η_L may depend on the system dimensionless numbers. The exponent in (4.14) is consistent with the predictions made for the special cases discussed above. Specifically, for $n = 1$ it is $(3\alpha + 1)/8$ as we predict in (4.2b), and for $\alpha = 5$ it is 2 independently of n as we predict in (4.8b). This similarity solution does not reveal the evolution of the fluid front r_N in the non-lubricated region, which depends on the fluid exponent n.

4.3.2. *The top layer 'liquid' limit, $\mathcal{M} \ll 1$*

The second asymptotic limit, $\mathcal{M} \ll 1$, in which the top fluid is much less viscous than the underlying fluid, also admits a similarity solution, but of a different subset of the model. In this case, the leading-order scaling of the power-law fluid local flux in the lubricated region (2.22a) is

$$q \approx -\mathcal{N} \frac{\partial H}{\partial r} \left| \frac{\partial H}{\partial r} \right|^{n-1} (H - h)^{2+n}, \tag{4.15}$$

which is identical to the scaling of the power-law fluid in the non-lubricated region (2.20a,b). Therefore, the evolution of the power-law fluid in the entire domain converges when $h \ll H$ to the similarity solution of a non-lubricated power-law GC, in which case the upper fluid front evolves with an n-dependent exponent

$$r_N = \eta_N \, \mathcal{N}^{1/(5n+3)} \, t^{(\alpha(2n+1)+1)/(5n+3)} \tag{4.16}$$

(Sayag & Worster 2013), where the intercept η_N may depend on the system dimensionless numbers. This similarity solution does not hold for the underlying fluid layer since the local flux of the Newtonian underlying fluid sets a different scaling. Therefore, it does not predict the evolution of the underlying fluid front r_L. For $H - h > 1$, the coupling between the upper fluid layer and the lower one grows stronger the more shear-thinning the fluid is ($n \to \infty$), as the exponent in (4.15) grows like n. Therefore, (4.16) is expected to be less accurate the more shear-thinning the upper fluid is when $H - h > 1$, and more accurate when $H - h < 1$.

4.4. *Asymptotic solutions in the vicinity of the fluid fronts*

The thicknesses of the two fluid layers in the vicinity of the fronts also have self-similar forms in the absence of a global similarity solution. These self-similar forms arise because the dynamics in the vicinity of both fronts is dominated by the same dynamics that governs non-lubricated GCs, which are known to have self-similar solutions for any α and n (Huppert 1982; Sayag & Worster 2013).

The dominance of a non-lubricated GC dynamics is naturally expected in the vicinity of the front r_N, which is the edge of the non-lubricated region in the flow. In this case, we expect consistency of the fluid thickness with Sayag & Worster (2013), which implies a similarity solution of the form

$$r = \eta \, t^{(\alpha(2n+1)+1)/(5n+3)}, \tag{4.17a}$$

$$H = t^{(\alpha(n+1)-2)/(5n+3)} \, F \left(\frac{\eta}{\eta_N} \right), \tag{4.17b}$$

for the model described by (2.19) and (2.20a,b). Therefore, the asymptotic solution for the function F near the front η_N in the similarity space is (Sayag & Worster 2013)

$$F = \left[N \eta_N^{n+1} \left(1 - \frac{\eta}{\eta_N} \right)^n \right]^{1/(2n+1)}, \quad N = \left(\frac{1}{\mathcal{N}} \frac{\alpha(2n+1)+1}{5n+3} \right)^{1/n} \frac{2n+1}{n}. \tag{4.18a,b}$$

Near the front r_L, the dominance of non-lubricated GC dynamics is also valid, but requires a more careful supporting argument. Specifically, we assert that the free surface slope

$\partial H / \partial r$ is finite at r_L, whereas the slope of the lubricating fluid is singular. Therefore, provided that the density difference is non zero, the leading-order flux q_ℓ (2.22b) becomes

$$q_\ell = -\frac{\mathcal{M}\mathcal{D}}{3} h^3 \frac{\partial h}{\partial r}. \tag{4.19}$$

Consequently, the model (2.21a) for the lubricating fluid near r_L is decoupled from H, and describes a modified non-lubricated GC of a Newtonian fluid (Huppert 1982). In this case, the thickness h has a similarity solution of the form

$$r = \eta(t - t_L)^{(3\alpha+1)/8}, \tag{4.20a}$$

$$h = (t - t_L)^{(\alpha-1)/4} f\left(\frac{\eta}{\eta_L}\right). \tag{4.20b}$$

Therefore, the asymptotic solution for the function f near the front η_L in the similarity space is (Huppert 1982)

$$f = \left[\frac{9(3\alpha+1)}{8} \frac{\eta_L^2}{\mathcal{M}\mathcal{D}} \left(1 - \frac{\eta}{\eta_L}\right)\right]^{1/3}. \tag{4.21}$$

Plugging the similarity solutions for the power-law fluid (4.17a) and for the Newtonian fluid (4.20a) into the dimensionless form of the global mass conservation equations (2.24), we get

$$2\pi \int_0^{\eta_N} (F - f)\eta \, \mathrm{d}\eta = 1, \tag{4.22a}$$

$$2\pi \int_0^{\eta_L} f\eta \, \mathrm{d}\eta = \mathcal{Q}, \tag{4.22b}$$

in the late-time limit $t/t_L \gg 1$, where we note that the time exponents in the first equation vanish even though the exponents in the non-Newtonian case have n dependence. Plugging the similarity solutions for F and f and solving, we obtain the closed-form solutions for the intercepts of the fronts:

$$\eta_N = \left[\frac{2\pi}{1 + \mathcal{Q}} \frac{(2n+1)^2}{(5n+2)(3n+1)} N^{n/(2n+1)}\right]^{-(2n+1)/(5n+3)}, \tag{4.23a}$$

$$\eta_L = \left[\frac{2\pi}{\mathcal{Q}} \frac{9}{28} \left(\frac{9(3\alpha+1)}{8\mathcal{M}\mathcal{D}}\right)^{1/3}\right]^{-3/8}. \tag{4.23b}$$

The asymptotic solutions (4.18a,b) and (4.21) that we obtain based on the asymptotic limit in which the two layers are decoupled appear to provide a precise prediction for the fluid thicknesses of the lubricated GC in the vicinity of the fronts when using the numerically calculated values for η_L, η_N of the lubricated GC (figure 5). The values for η_L and η_N in (4.23), based on the non-lubricated GC solution, provide a rough estimate for those of the lubricated GC. Discrepancies between the two seem to decline the more shear-thickening ($n < 1$) and the less lubricated the upper layer ($\mathcal{M} \ll 1$) is (figure 6a). These discrepancies could be due to differences in the predicted thickness structure near the fluid fronts. Specifically, the more shear-thinning the fluid, the sharper the fluid front region, as implied by the thickness structure $F \sim (1 - \eta/\eta_N)^{n/(2n+1)}$ (see (4.18a,b)).
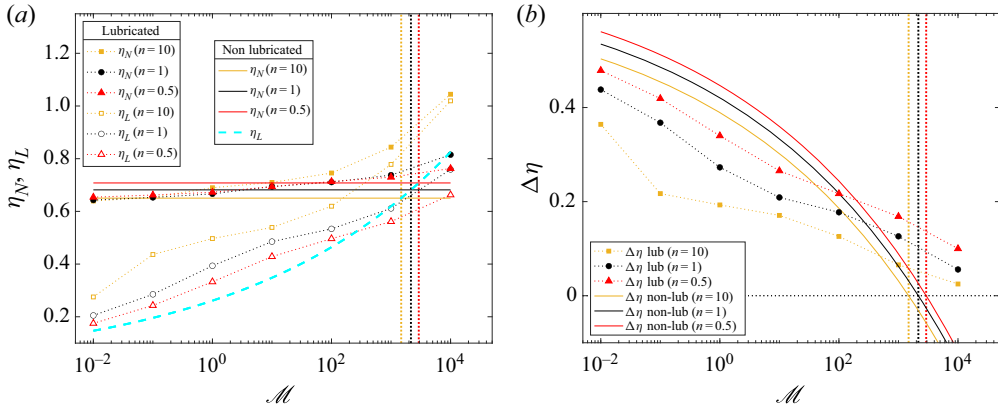
949 A40-16

Figure 6. (*a*) The coefficients η_N, η_L of the lubricated GC solutions compared with those of the asymptotic solution near the fronts given by the non-lubricated GC similarity solutions, where $\mathcal{Q} = 0.2$, $\mathcal{D} = 0.1$, $\alpha = 1$, $10^{-2} \leqslant \mathcal{M} \leqslant 10^4$, and $n = 10, 1, 0.5$. The η_N of the asymptotic solutions (solid lines) are independent of $\mathcal{M}$ and diminish with n, whereas those of the lubricated GC (solid markers at corresponding colours) are nearly equal in the liquid limit ($\mathcal{M} \ll 1$) and grow monotonically with $\mathcal{M}$. The corresponding η_L of the asymptotic solution (dashed cyan line) are independent of n, unlike those of the lubricated GC solution (hollow markers), but both grow monotonically with $\mathcal{M}$. Vertical grid lines mark the threshold viscosity ratio $\mathcal{M}_c$ based on the non-lubricated GC solutions. (*b*) The difference $\Delta\eta \equiv \eta_N - \eta_L$ of the lubricated and non-lubricated values in (*a*).

Consequently, the more shear-thinning the fluid, the more the predicted thickness F in the lubricated region overestimates the numerical solution (compare figures 5*a*,*c*), and by global mass conservation (see (4.22)), the smaller the predicted η_N compared to the numerical value.

5. Front outstripping

In the absence of global similarity solutions, the fronts propagate at different rates, implying that under certain conditions, the inner lubricating front r_L may outstrip the outer front r_N. We identify two outstripping mechanisms, one driven by the solution intercepts at early time, and the other by the exponents at late time.

5.1. *Intercept outstripping*

When the lubricating fluid emerges, $t - t_L \gtrsim 0$, the growth of its front is dominated by the intercept η_L, whereas the contribution of the power-law growth $(t - t_L)^{\beta_L}$ is relatively small. Therefore, the outstripping of $r_N(t)$ by $r_L(t)$ can occur faster the larger η_L is compared to η_N. The intercept difference $\Delta\eta \equiv \eta_N - \eta_L$ predicted by the asymptotic, non-lubricated GC solution (4.23) diminishes with $\mathcal{M}$ and becomes negative when $\mathcal{M}$ grows beyond a threshold value that we denote by $\mathcal{M}_c$ (figure 6*b*). This implies that across that threshold in the viscosity ratio, $\eta_L > \eta_N$ and the lubricating front can outstrip the upper fluid front. The threshold viscosity ratio $\mathcal{M}_c$ is found by setting $\Delta\eta = 0$ and solving for $\mathcal{M}$, to get

$$\mathcal{M}_c \equiv \left(\frac{2\pi}{\mathcal{Q}}\frac{9}{28}\right)^3 \left(\frac{9(3\alpha + 1)}{8\mathcal{D}}\right) \left[\frac{1 + \mathcal{Q}}{2\pi}\frac{(5n + 2)(3n + 1)}{(2n + 1)^2} N^{-n/(2n+1)}\right]^{8(2n+1)/(5n+3)}.$$
(5.1)

Therefore, in the purely Newtonian case, the threshold viscosity ratio is

$$\mathscr{M}_c(n=1) = \frac{1}{\mathscr{D}}\left(1 + \frac{1}{\mathscr{Q}}\right)^3, \tag{5.2}$$

which is independent of α. In the case of constant flux $\alpha = 1$, the threshold is

$$\mathscr{M}_c(\alpha = 1) = \left(\frac{2\pi}{\mathscr{Q}}\frac{9}{28}\right)^3 \frac{9}{2\mathscr{D}}\left[\frac{1+\mathscr{Q}}{2\pi}\frac{(5n+2)(3n+1)}{(2n+1)^2}N^{-n/(2n+1)}\right]^{8(2n+1)/(5n+3)}. \tag{5.3}$$

This behaviour, which is reasoned based on the asymptotic, non-lubricated GC solution, is consistent with the trend of the full lubricated GC solution (figure 6b). We note that we do not explicitly observe an outstripping of the outer front by the inner one since the simulation involves the constraint $r_L < r_N$.

5.2. *Exponent outstripping*

Another mechanism of outstripping can arise due to the different time exponents of the two fronts. This difference can be evaluated by the similarity solutions in the vicinity of the fronts. Specifically, denoting the front exponents by $\beta_N \equiv [\alpha(1+2n)+1]/(5n+3)$ (see (4.17a)) and $\beta_L \equiv (3\alpha+1)/8$ (see (4.20a)), we have

$$\Delta\beta \equiv \beta_L - \beta_N = \frac{(5-\alpha)(n-1)}{8(5n+3)}. \tag{5.4}$$

When the flow has a global similarity solution ($\alpha = 5$ or $n = 1$), the exponents of the two fluid fronts are identical, $\Delta\beta = 0$, implying that asymptotically in time, the gap between the two fronts evolves with the same exponent, and the ratio of their positions r_L/r_N is constant. When $n \neq 1$ and $\alpha \neq 5$, there is no global similarity solution, implying that $\beta_L \neq \beta_N$ and that the fronts ratio evolves proportionally to $t^{\Delta\beta}$. Consequently, the gap between the fronts closes down in time, and front outstripping occurs when $\Delta\beta > 0$, which is when $\alpha < 5$ and $n > 1$, or when $\alpha > 5$ and $n < 1$ (figure 7). When $\Delta\beta < 0$, intercept outstripping does not occur through exponent outstripping, but can still occur through intercept outstripping at early time ($t/t_L \gtrsim 1$) when $\mathscr{M} > \mathscr{M}_c$.

6. Solutions for constant flux discharge $\alpha = 1$

The case of constant flux ($\alpha = 1$) was explored theoretically in several asymptotic limits, including the case of no lubrication (Huppert 1982; Sayag & Worster 2013) and the case where both fluids are Newtonian (Kowal & Worster 2015). These cases are useful to validate our general solutions in several asymptotic limits and to elucidate the impact of lubrication when the upper fluid is non-Newtonian.

When the upper fluid is Newtonian ($n = 1$), the flow is self-similar and can be classified into four different flow regimes in the $\mathscr{M}$–$\mathscr{Q}$ state space (Kowal & Worster 2015), in which the radial distribution of the fluid thickness and the evolution of the fronts have unique qualitative characteristics (figures 8 and 9). When the upper fluid is non-Newtonian ($n \neq 1$), no global similarity solution arises for a constant flux discharge (§ 2.3). Nevertheless, we find numerically that the characteristic distributions of the fluid thickness in each of the four regimes are preserved qualitatively (figure 9). Moreover, the
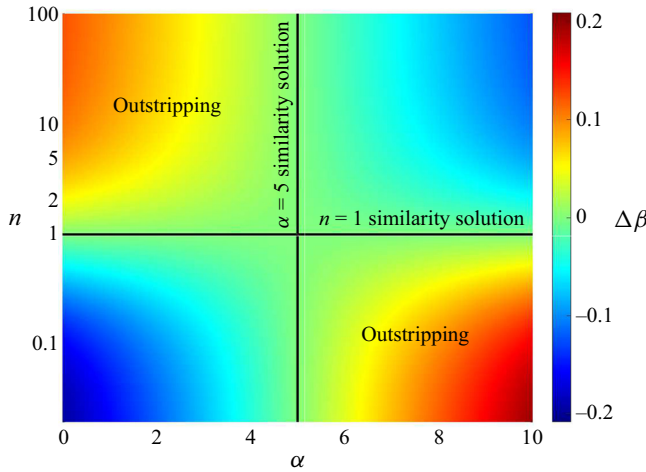
Figure 7. The exponent difference $\Delta\beta$ as a function of the fluid discharge exponent α and the viscosity exponent n. Dark lines are the $\Delta\beta = 0$ contours, where global similarity solutions exist. When $\Delta\beta > 0$ (hot colours), the lubricating fluid front r_L outstrips the non-Newtonian fluid front r_N.

thickness of the lubricating fluid in the non-Newtonian case varies very weakly from that in the purely Newtonian case, and the fronts r_L in both cases appear to follow a similar evolution pattern (figure 9). In contrast, the propagation rate of the front r_N varies strongly with the non-Newtonian properties of the upper fluid, becoming faster than the purely Newtonian case for shear-thickening fluids, and slower than the purely Newtonian case for shear-thinning fluids (figure 9). This pattern in all of the four regimes can be rationalized physically through a dimension-based argument: the radial velocity at constant flux $[u] \sim Q/(2\pi RH)$ combined with the thickness scale $[H] \sim (Q\mu_\ell/\rho g)^{1/4}$ (see (2.26c)) implies that the dominant strain rate $[\partial u/\partial z] \sim Q/(2\pi RH^2) \sim (\rho g Q/\mu_\ell)^{1/2}/(2\pi R)$ declines radially. Consequently, a shear-thinning fluid ($n > 1$) becomes increasingly more viscous with radius than a shear-thickening fluid, leading to its relatively slower propagation.

The slower front speed of a shear-thinning fluid compared to a Newtonian fluid implies that outstripping by the front of the Newtonian lubricating fluid may occur after some time (§ 5). We investigate this more carefully by considering the evolution of the two fronts within a range of viscosity ratios $10^{-2} \leqslant \mathcal{M} \leqslant 10^4$, a range of fluid exponent $n = 10, 1, 0.5$, and for fixed flux ratio $\mathcal{Q} = 0.2$, density ratio $\mathcal{D} = 0.1$, and $\alpha = 1$. Even though no global similarity solution of the first kind exists when $n \neq 1$, we find that each front has a power-law evolution in time of the form

$$r_N(t) \approx c_N t^{\beta_N}, \quad r_L(t) \approx c_L(t-1)^{\beta_L}. \quad (6.1a,b)$$

We compute the intercepts c_N, c_L and the exponents β_N, β_L through regression to the numerical solution (figures 10, 11 and 12). In the upper fluid 'liquid' limit, $\mathcal{M} \ll 1$, we find that the numerical solution for the front of the upper fluid evolves consistently with (4.16), in which $\beta_N = (2 + 2n)/(5n + 3)$ and $c_N = \eta_N \mathcal{N}^{1/(5n+3)}$. For example, when $\mathcal{M} = 0.01$, the computed exponents β_N for $n = 0.5, 1, 10$ differ from the corresponding theoretical values $6/11, 1/2, 22/53$ by less than 2 % (figures 10a, 11a). The larger discrepancy among those is for the shear-thinning fluid, which is expected due to the stronger coupling in this case between the upper and the lower fluid layers, as mentioned in § 4.3.2. The corresponding intercept c_N differs by less than 5 % from the theoretical values (figure 11d). The exponent β_L is $\approx 1/2$ for $n = 1$, larger than 1/2 for a shear-thinning
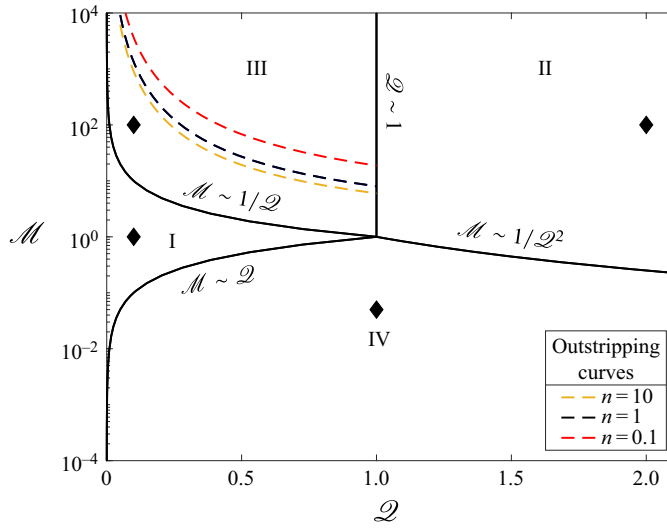
Figure 8. The $\mathcal{M}$–$\mathcal{Q}$ state map for $\alpha = 1$, $n = 1$ and $\mathcal{D} = 1$ is divided into four characteristic flow regimes, I–IV. The dashed curves mark the critical viscosity ratios $\mathcal{M}_c(\mathcal{Q}, n)$ from (5.3), beyond which we expect the front of the lubricating fluid to outstrip the front of the top fluid. The characteristic solution of the $\mathcal{M}$–$\mathcal{Q}$ states marked by diamonds are shown in figure 9.
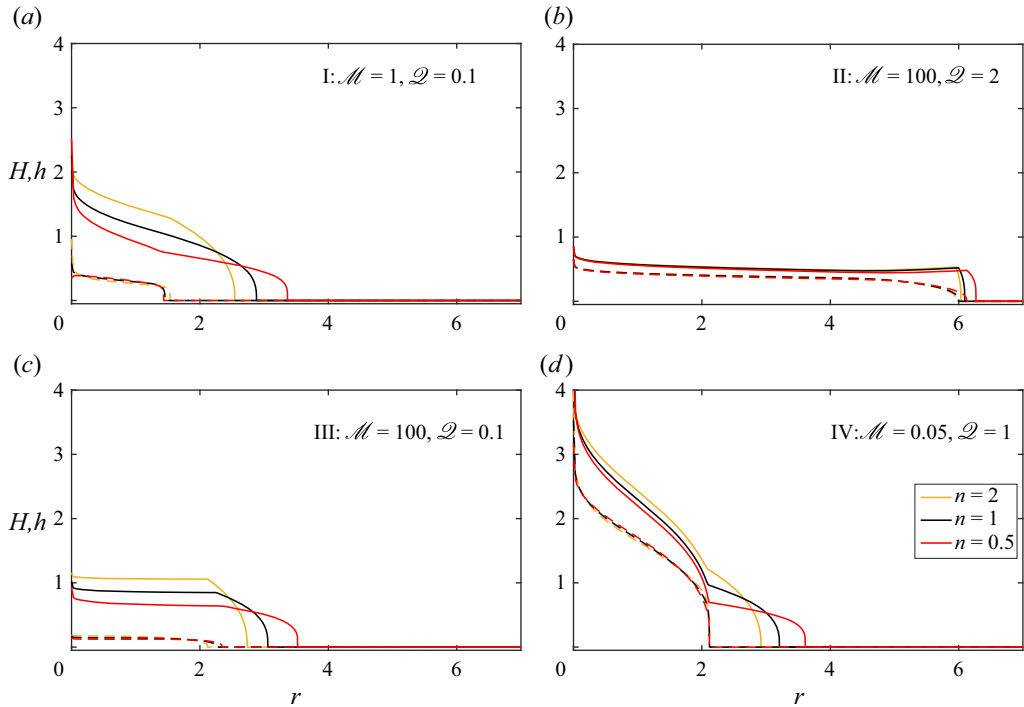

Figure 9. Characteristic solutions of each of the four states in the different regimes marked by diamonds in figure 8 for a range of power-law exponents (yellow $n = 2$, black $n = 1$, and red $n = 0.5$), at constant flux ($\alpha = 1$), showing the position of the free surface of the lubricated power-law fluid (solid lines), and the lubricating Newtonian fluid (dashed lines), at constant dimensionless time $t = 20$, and $\mathcal{D} = 1$.
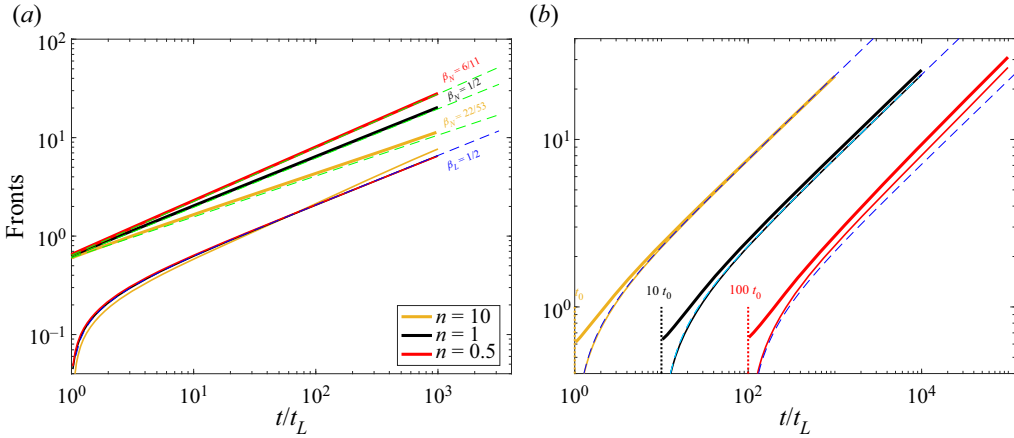
Figure 10. The non-dimensional front positions r_N (thick solid lines) and r_L (thin solid lines) for power-law fluid exponents, $n = 10, 1, 0.5$, and for $\alpha = 1$, $\mathcal{Q} = 0.2$ and $\mathcal{D} = 0.1$. (a) Here, $\mathcal{M} = 0.01$. Shown for reference are the theoretical prediction for $r_N(t)$ (4.16) in the $\mathcal{M} \ll 1$ limit (green dashed), and the prediction for the purely Newtonian solution (blue dashed). (b) Here, $\mathcal{M} = 10^4 > \mathcal{M}_c(n)$. Shown for reference are curves with exponent $1/2$ (blue dashed), corresponding to the purely Newtonian solution. The exponents of each front are $\beta_N = 0.4962 \pm 0.0006$, 0.5 ± 0.001, 0.523 ± 0.003 and $\beta_L = 0.4984 \pm 0.0001$, 0.4998 ± 0.0003, 0.526 ± 0.002 for $n = 10, 1, 0.5$, respectively.

fluid (by 10 % for $n = 10$), and smaller than $1/2$ for shear-thickening fluid (by 1.2 % for $n = 1/2$) (figures 10b, 11b). The corresponding intercept c_L has small variation with n, being in the range $0.17 \lesssim c_L \lesssim 0.21$, which is much smaller than the intercept in Newtonian non-lubricated GCs, $\eta_L(1/3)^{1/8} \approx 0.62$ (figure 11e).

In the upper fluid 'solid' limit, $\mathcal{M} \gg 1$, we find that the front of the lubricating fluid evolves consistently with (4.14), in which $\beta_L \to 1/2$ is n-independent, and the solution for β_N also tends to $1/2$ (figures 10b, 11a,b). We note again that when $\mathcal{M} > \mathcal{M}_c$, the results of the simulation are questionable, as theoretically we expect front outstripping, which our simulation is not built to resolve. For intermediate $\mathcal{M}$ values we find that the front exponent β_N varies weakly with $\mathcal{M}$ initially ($\mathcal{M} \lesssim 10$), remaining close to the $\mathcal{M} \ll 1$ asymptotic values (figure 11a), and the intercept c_N grows with $\mathcal{M}$ and varies weakly with n (figure 11d). The exponent of the lubricating front β_L grows with $\mathcal{M}$ over $1/2$ for shear-thickening fluids and less than $1/2$ for shear-thinning fluids (figure 11b), whereas the intercept c_L grows monotonically with $\mathcal{M}$ for all n values while varying very weakly with n (figure 11e).

Throughout the range $10^{-2} \leqslant \mathcal{M} \leqslant 10^4$, we find that $\Delta\beta < 0$ for shear-thickening fluids, $\Delta\beta > 0$ for shear-thinning fluids, and $\Delta\beta = 0 \pm 0.0008$ for Newtonian fluids (figure 11c), consistently with our predictions using the similarity solutions near the front (§ 5.2). This implies that in the long-time limit, the front r_L outstrips r_N when the upper fluid is shear-thinning, independently of $\mathcal{M}$, while no exponent outstripping is expected when the upper fluid is shear-thickening. Simultaneously, the intercept difference $c_N - c_L$ is positive throughout the range of $\mathcal{M}$ but approaches zero in the vicinity of $\mathcal{M} = 10^3 \approx \mathcal{M}_c(n)$ (figure 11f). This may reflect the approach to an intercept-driven outstripping ($c_N - c_L < 0$) across the critical viscosity ratio $\mathcal{M} > \mathcal{M}_c(n)$. The classification of the $\alpha = 1$ simulations to the two outstripping mechanisms is presented in figure 12.
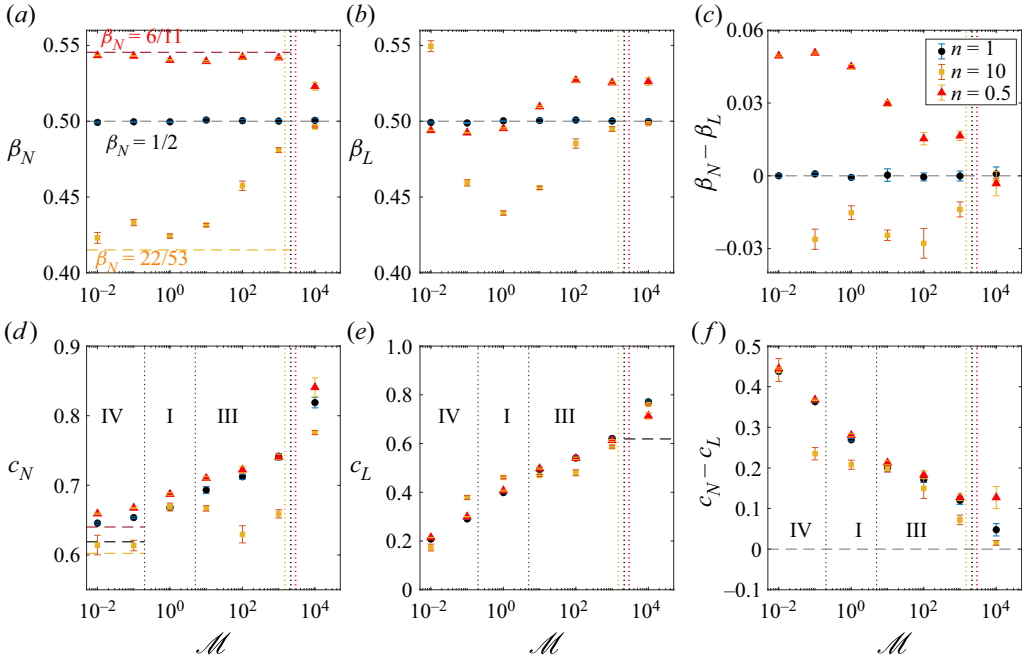
Figure 11. The fitted exponents and intercepts to numerical solutions of the fronts r_N, r_L for varying $\mathcal{M}$, $n = 10, 1, 0.5, \alpha = 1, \mathcal{Q} = 0.2$ and $\mathcal{D} = 0.1$. Vertical grid lines (dotted) mark the intercept-driven outstripping threshold $\mathcal{M}_c(n)$. (*a*) The exponent β_N, with the predicted asymptotic ($\mathcal{M} \ll 1$) exponents $(2n + 2)/(5n + 3)$ (see (4.16); horizontal gridlines) corresponding by colour to the specific n. (*b*) The exponent β_L, with the predicted exponent for $n = 1$ (horizontal gridline; Kowal & Worster 2015). (*c*) The exponent difference $\beta_N - \beta_L$, with horizontal gridlines representing the threshold for outstripping. (*d*) The intercept c_N, with the predicted asymptotic ($\mathcal{M} \ll 1$) intercepts (horizontal gridlines) $\eta_N \mathcal{N}^{1/(5n+3)}$ (see (4.16)) corresponding by colour to the specific n values. (*e*) The intercept c_L, with the asymptotic intercept of a Newtonian non-lubricated GC (horizontal gridline) $\eta_L(1/3)^{1/8}$ (Huppert 1982). (*f*) The intercept difference $c_N - c_L$, with the threshold for intercept outstripping (horizontal gridlines). Vertical gridlines (grey) in (*d*–*f*) mark the regime thresholds (see figure 8).

7. Comparison with experimental evidence for $\alpha = 1$ and $n > 1$

The theory that we have developed can be validated with the recent laboratory experiments of lubricated GCs (Kumar *et al.* 2021). The experiments consisted of a strain-rate softening fluid (xanthan gum solution, $n > 1$) that was lubricated by a denser Newtonian fluid (sugar solution). Both fluids were released at constant flux ($\alpha = 1$) over a glass plane, which had surface conditions very close to no-slip, as validated through non-lubricated GC experiments and theory (Sayag & Worster 2013; Kumar *et al.* 2021).

The results obtained from fifteen lubricated GC experiments (table 1) that lasted over $10 \, t_L$ in some cases, and with flux ratio $\mathcal{Q} \lesssim 0.06$, have shown that both fronts were highly axisymmetric, implying that compliance with our assumptions of axisymmetric flow should be valid. As we noted earlier, our theory has utilized the lubrication approximation, implying that it is valid as long as the thickness-to-radius aspect ratio is sufficiently small. We can estimate the instant when the flows satisfy the lubrication approximation by requiring the ratio $r/h \gtrsim 10$ for each fluid. We assume that the instantaneous fluid volume in each layer is distributed in a disc of radius r_i, where i represents the upper or lower fluid, of thickness $h_i = Q_i t^\alpha / \pi r_i^2$. This implies that the lubrication approximation is valid as soon as $r_N(t)^3/t \gtrsim 10Q/\pi$ for the top fluid and $r_L(t)^3/(t - t_L) \gtrsim 10Q_\ell/\pi$ for the lubricating fluid, where r_N, r_L were measured experimentally.
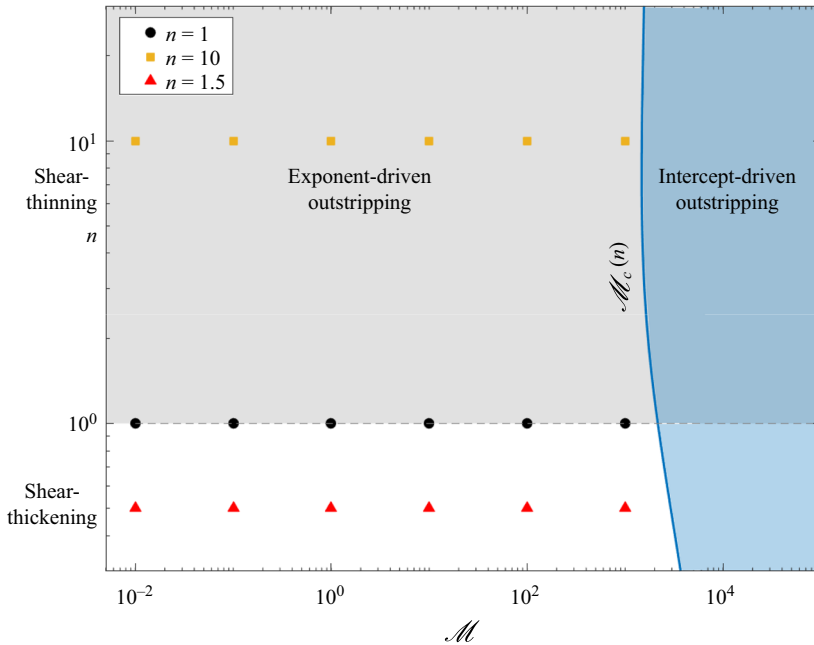
949 A40-22

Figure 12. The $\mathcal{M}$–n state map for $\alpha = 1$, $\mathcal{Q} = 0.2$ and $\mathcal{D} = 0.1$, showing the numerical simulations presented in figure 11 (markers). The region in cyan bounded by the curve $\mathcal{M}_c(n)$ is where intercept outstripping occurs. The region in grey bounded by $n = 1$ is where exponent outstripping occurs.

Experiment	$\mathcal{Q}$	$\mathcal{M}$	c (%/w)
1 ◆	0.0574	7661	1
2 ▲	0.0283	6936	1
3 ▼	0.04697	6006	1
4 ●	0.0223	4671	2
5 ■	0.0218	42 717	2
6 ▶	0.0222	5023	2
7 ◀	0.0222	23 639	2
8 ★	0.0223	10 412	2
9 ✦	0.022	17 036	2
10 ●	0.022	17 323	2
11 ■	0.0333	24 661	2
12 ◆	0.03	23 017	2
13 ▲	0.0217	41 528	2
14 ▼	0.0218	43 483	2
15 ▶	0.0541	24 343	2

Table 1. The lubricated GC experiments (Kumar *et al.* 2021, table 1c) were performed at constant flux ($\alpha = 1$), with power-law fluids having two different polymer concentrations (third column), corresponding to one fluid ($c = 1\%$) with exponent $n = 6.14$ and reduced density ratio $\mathcal{D} = 0.156$, and a second fluid ($c = 2\%$) with exponent $n = 7.14$ and reduced density ratio $\mathcal{D} = 0.152$.

7.1. *Propagation of the fronts*

Experimentally, it was found that the two fronts evolved faster than those of non-lubricated GCs of the corresponding fluids. Nevertheless, each front had a power-law time evolution with a similar exponent as non-lubricated GCs of the corresponding fluids. In particular,
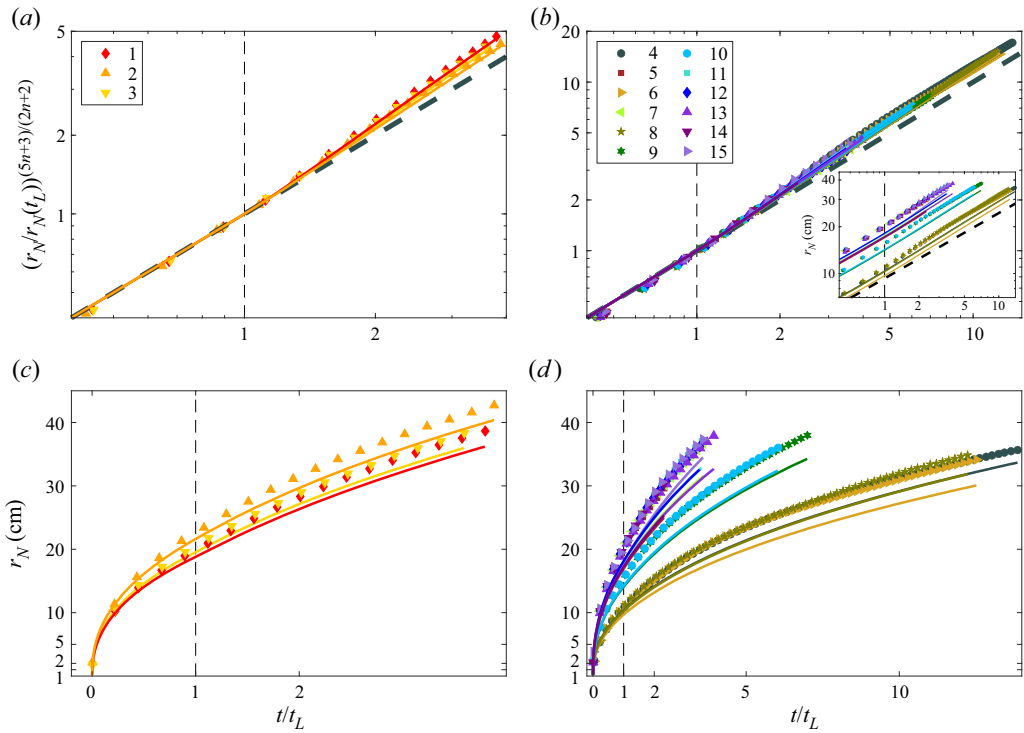
Figure 13. Comparison of the theoretical predictions of the fronts r_N evolution (coloured lines) with the experimental measurements (markers) (Kumar *et al.* 2021, and table 1). (*a,c*) Comparison with the 1 % polymer concentration (experiments 1–3) in logarithmic and linear scales, respectively. In (*a*), the fronts are normalized with the similarity solution of non-lubricated GCs of power-law fluids (Sayag & Worster 2013), and the front solution of such a current is shown for reference (grey dashed line). (*b,d*) Same as (*a,c*) but for experiments 4–15 of the 2 % polymer concentration. Inset in (*b*) zooms into the late-time regime (unscaled values) to present more clearly the experimental versus numerical results.

the front r_N evolved with exponent $(2n+2)/(5n+3) \approx 0.42$ before the lubrication fluid was introduced ($t \leqslant t_L$), and then with a larger exponent approximately 0.46 ± 0.02. At $t \gtrsim 5t_L$, the exponents appeared to diminish and recover the early-time value. At the same time, the front r_L evolved consistently with exponent $1/2$ (Kumar *et al.* 2021).

To compare our theoretical predictions to the experimental measurements, we compute numerical solutions to each of the 15 experiments described in Kumar *et al.* (2021) based on the measured quantities $\mathcal{Q}$, $\mathcal{M}(\mathcal{T})$, $\mathcal{D}$ and n (table 1), where the time scale $\mathcal{T}$ was set as t_L and without fitting any parameter (figures 13 and 14). The viscosity ratio in each of these experiments was in the range $1 \ll \mathcal{M} < \mathcal{M}_c$, implying that the experiments were all in the exponent outstripping regime (§ 5.2), as well as in the solid-limit regime (§ 4.3.1), which predicts lubrication-front evolution like $r_L \propto t^{1/2}$.

Comparing the time exponents, we find that the numerical solutions and the theoretical predictions are consistent to leading order with those measured experimentally for both r_N (figures 13*a,b*) and r_L (figures 14*a,b*). Specifically, during $t \lesssim t_L$, the solutions to the front r_N evolve with the non-lubricated GC exponent $(2n+2)/(5n+3) \approx 0.42$. After the initiation of lubrication during $t \gtrsim t_L$, solutions to the front r_N evolve with a larger exponent, consistent with the experimental measurement (figures 13*a,b*). Such larger exponents than the non-lubricated GC value are consistent with our earlier result in
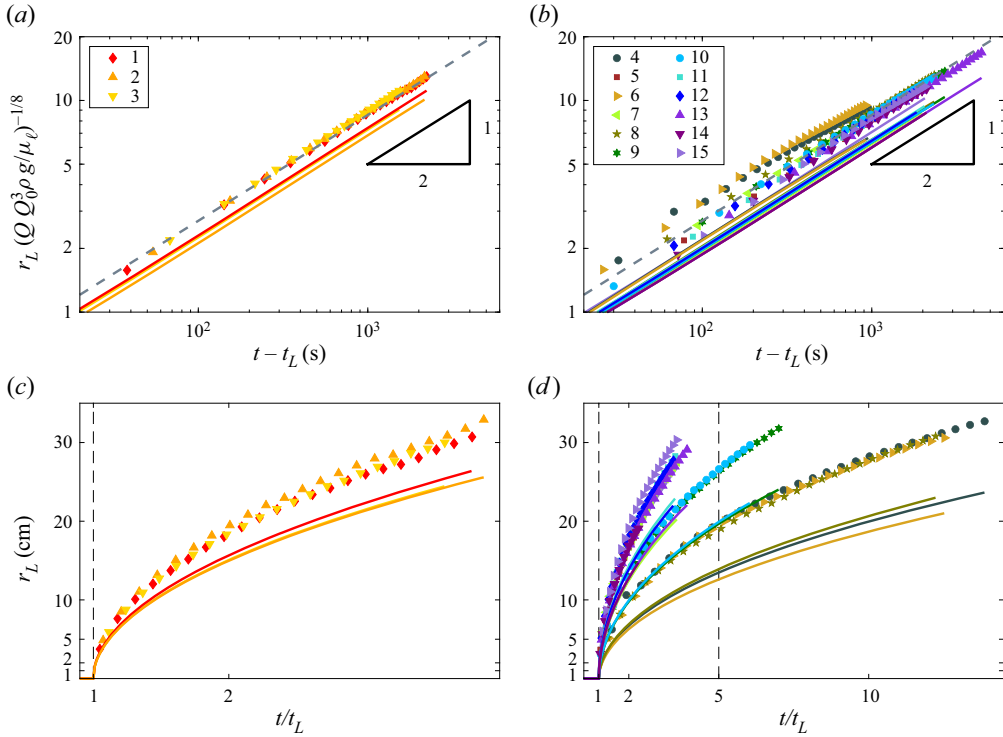
949 A40-24

Figure 14. Comparison of the theoretical predictions of the fronts r_L evolution (coloured lines) with the experimental measurements (markers) (Kumar *et al.* 2021, and table 1). (*a,c*) Comparison with the 1 % polymer concentration (experiments 1–3) in logarithmic and linear scales, respectively. In (*a*), the fronts are normalized with the similarity solution of a Newtonian lubricated GC (Kowal & Worster 2015), and the front solution of such a current is shown for reference (grey dashed line), with fitted coefficient 0.27. (*b,d*) Same as (*a,b*), but for experiments 4–15 of the 2 % polymer concentration.

figure 11(*a*) for $\mathcal{M}$ values close to $\mathcal{M}_c$. These higher exponents persist also at $t \gtrsim 5t_L$ and do not appear to diminish as argued for some of the experimental measurements (figure 13*b*, inset). We believe that the experimental measurements do not extend long enough to confidently determine inconsistency between the numerical calculation and the experiments during the late-time evolution. The solutions to the front r_L evolve with exponent 1/2, consistently with the experimental measurements (figures 14*a,b*). In spite of this consistency, the experimental fronts advance faster than the predicted ones (figures 13*c,d* and 14*c,d*), which implies that the intercepts that were predicted numerically are lower than those that were measured experimentally. This discrepancy is larger in experiments with higher polymer concentration (figures 13*d* and 14*d*). Therefore, additional physical processes that contribute to a faster front propagation are not accounted for by our theoretical model. We elaborate on potential important mechanisms in § 8.

7.2. *Thickness evolution*

The raw thickness signal of the non-Newtonian fluid that was measured experimentally from light transmitted through the fluid layers (Kumar *et al.* 2021) was biased and noisy, partially due to white noise that originated in the light detector along the entire measurement domain. We accounted for this by offsetting the signal by the average value
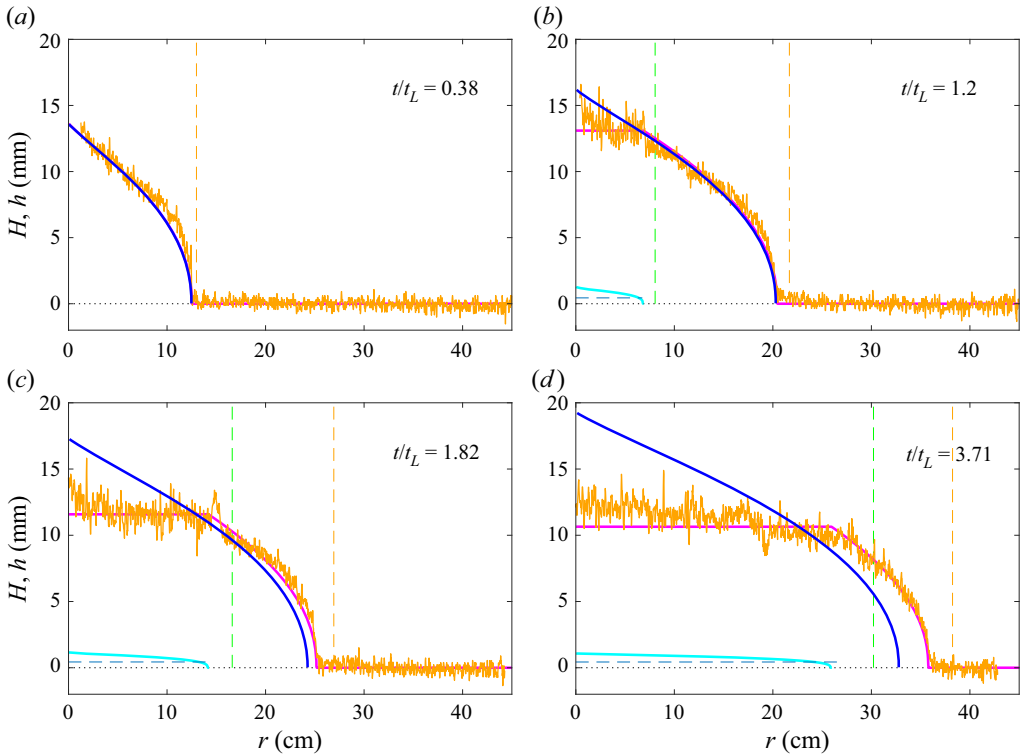
Figure 15. Comparison of the numerical solution of the top fluid thicknesses (magenta solid line) with the experimental measurements (experiment 1 in Kumar *et al.* (2021) and table 1, orange solid line), at four different instants ranging from the non-lubricated phase (*a*) through the lubricated phase (*b–d*). The experimental data were translated so that the front r_N matches with the numerical value in order to focus the comparison of the GC shapes. The corresponding thickness solutions of non-lubricated GCs of power-law fluid (Sayag & Worster 2013) are shown for reference (blue solid line). Also shown are the corresponding numerical solutions for the lubrication layer (cyan solid line), and the average thickness measured in the experiment, $h_\ell \approx 0.43$ (pale blue dashed line). Vertical grid lines mark the average instantaneous positions of the experimentally measured fronts r_N (orange) and r_L (green).

of the noise at the fluid-free region $r > r_N$ (figure 15). Another source of signal noise in the lubricated domain ($r < r_L$) represents thickness variations in the non-Newtonian fluid due to roughness of the fluid–fluid interface. This rough structure is also evident in the lubricating fluid colour variations throughout the lubrication fluid domain (figure 1), which may have resulted from an interfacial instability along the fluid–fluid interface (Kumar *et al.* 2021). The noise at the free surface had a small amplitude compared with the thickness of the top fluid layer, which turned out nearly uniform in the lubricated region. The layer of the lubricating fluid was also largely uniform with localized spikes, and its average thickness was approximated through mass conservation to be $h_\ell = Q_\ell(t - t_L)/\rho_\ell \pi r_L^2 \approx 0.43$ mm (Kumar *et al.* 2021). These nearly uniform patterns differ substantially from the monotonically diminishing thickness of non-lubricated GCs under similar conditions.

To compare the thickness distribution and particularly the shape of the fronts, we remove the difference in the front positions that was discussed separately in § 7.1, by horizontal translation of the experimental signal so that its front $r_N(t)$ coincides with that

949 A40-26

computed numerically. Consequently, we find that the thickness distribution predicted by our numerical solutions, which do not involve any fitting parameter, are highly consistent with the experimental measurements along a wide range of instants (figure 15).

8. Discussion

The lubricated GCs that we consider involve five dimensionless parameters, $\mathscr{Q}$, $\mathscr{D}$, $\mathscr{M}$, n and α, associated with significant qualitative transitions in the structure of the solution, in the relative motion of the fluid fronts and their stability, and in the thickness distribution of the two fluids.

The fluid exponent n and the discharge exponent α have a dramatic qualitative impact on the solutions. Specifically, similarity solutions exist only when $n = 1$, in which both fluids follow a similar constitutive law, and when $\alpha = 5$. In those cases, the two fronts evolve with the same power law in time, and as a result, the ratio r_N/r_L is constant. In all other cases ($n \neq 1$, $\alpha \neq 5$) the fronts also appear to follow a power-law evolution, but each with a different exponent, implying that asymptotically in time, the ratio r_N/r_L evolves following a power law in time with exponent $\Delta\beta$ from (5.4). Therefore, there are solutions where r_N/r_L declines in time resulting in the lubrication front outstripping the front of the upper fluid ($n > 1$ and $\alpha < 5$, and $n < 1$ and $\alpha > 5$), and otherwise r_N/r_L grows in time (figure 7).

The flux ratio $\mathscr{Q}$ can lead to the emergence of two significantly different patterns, and may have a critical impact on the front stability. When $\mathscr{Q} < 1$, the flux of the lubricating fluid is lower than the top fluid layer. Consequently, the thickness of the lubricating layer is significantly smaller, and the propagation of the front r_L is affected by the relatively larger pressure imposed by the thicker top layer (figures 9c and 15). The opposite occurs when $\mathscr{Q} > 1$ – the lubricating fluid is discharged at a larger flux, and its thickness is significantly larger than the top fluid layer (figure 9b). Moreover, $\mathscr{Q}$ may have a crucial impact on the stability of the axisymmetric fronts. Preliminary experimental evidence indicates that when the flux is constant ($\alpha = 1$), the top fluid layer is strain-rate softening ($n = 6$) and $\mathscr{M} \gg 1$, the initially axisymmetric fronts become unstable when $\mathscr{Q} \gtrsim 0.1$ and develop fingering patterns after an initial axisymmetric spreading (Kumar *et al.* 2021). Similar symmetry breaking has also been observed in the purely Newtonian case for $0.14 \lesssim \mathscr{Q} \lesssim 0.44$ (Kowal & Worster 2015).

The viscosity ratio $\mathscr{M}$ affects the relative motion of the fronts, and the relative thickness of the fluid layers. At a high viscosity ratio ($\mathscr{M} \gg 1$), the more viscous top fluid is effectively solid-like compared with the less viscous lower fluid. Consequently, the flow in the lubricated region is independent of the fluid exponent n, and both fluid layers in that region follow the same similarity solution, in which the front of the lubrication fluid r_L evolves with a time exponent $(3\alpha + 1)/8$, the same as a Newtonian non-lubricated GC (4.14). In the low viscosity ratio ($\mathscr{M} \ll 1$), the top fluid is significantly more mobile than the lower fluid layer, which does not provide an effective lubrication. In this case, the two fluid layers in the lubricated region do not exhibit a global similarity solution, but the top fluid layer along the whole domain does. Consequently, a self-similar solution exist in the top fluid layer, in which the front r_N evolves with a time exponent $[\alpha(2n + 1) + 1]/(5n + 3)$, the same as a non-lubricated GC (see (4.16)). The impact of the viscosity ratio on the fluid thickness distributions can be appreciated through the constant flux case ($\alpha = 1$), in which the free surface of the top fluid is substantially flatter in the $\mathscr{M} \gg 1$ case than in the $\mathscr{M} \lesssim 1$ case (figure 9).

Independently of the values of the dimensionless parameters, the solutions in the vicinity of the fronts are also self-similar, with exponents consistent with those of non-lubricated GCs of power-law fluids (Huppert 1982; Sayag & Worster 2013). In particular, both fronts evolve with an exponent $[\alpha(2n+1)+1]/(5n+3)$, which simplifies to $(3\alpha+1)/8$ for the Newtonian lubricating fluid. The intercepts of the front solutions depend on the different dimensionless numbers of the system. Together, the exponents and the intercepts provide insights into the interaction between the two fronts. One important consequence of that interaction is the outstripping of the upper fluid front by the lower lubricating fluid front, which can occur either through the intercept difference $\Delta\eta$ or through the exponent difference $\Delta\beta$. The condition for an intercept outstripping can be formalized in terms of the critical viscosity ratio $\mathscr{M}_c(\mathscr{Q}, \mathscr{D}, \alpha, n)$ (see (5.2)), so that outstripping occurs when $\mathscr{M} > \mathscr{M}_c$. Physically, this implies that when $\mathscr{Q} \ll 1$, $\mathscr{M}_c \propto 1/\mathscr{Q}^3 \gg 1$ and the top fluid should be significantly more viscous than the lower fluid for outstripping to occur, in which case the top fluid deforms substantially slower making it easier for the lubricating fluid front to outstrip. Alternatively, when $\mathscr{Q} \gg 1$, for shear-thinning fluids $\mathscr{M}_c(n \to \infty) \propto \mathscr{Q}^{1/5} \gg 1$, whereas for shear-thickening fluids $\mathscr{M}_c(n \to 0) \propto 1/\mathscr{Q}^{1/3} \ll 1$. When $\mathscr{M} < \mathscr{M}_c$, $\Delta\eta > 0$ and outstripping can be driven only by the exponents' difference. As discussed above, the condition for that mechanism depends on the values of n and α (figure 7). For example, shear-thinning fluids at relatively low discharge exponent ($\alpha < 5$) become increasingly more viscous as they expand radially, resulting in slower front velocity than the lubricating fluid front. Moreover, their thickness, and correspondingly the pressure they apply on the lubricating fluid, is relatively larger and contributes further to the radial spreading of the lubricating fluid. We find that the intercept-driven outstripping can occur significantly faster and relatively closer to t_L than the exponent-driven outstripping. For example, as in the constant flux ($\alpha = 1$) case, intercept-driven outstripping occurs at roughly $t/t_L \lesssim 10$, which is much faster than the $t/t_L \gtrsim 10^3$ in the exponent-driven case (figure 10).

It is important to note that the global similarity solution that we find for a discharge exponent $\alpha = 5$ arises in additional axisymmetric GCs of different settings, which *a priori* appear remotely related. This includes, for example, isothermal lava domes that are modelled as axisymmetric GCs of viscoplastic fluids (Balmforth *et al.* 2000). The structure of the similarity solution in that case is identical to the lubricating GCs that we consider, in which the front evolves like $r \propto t^2$, and the fluid thickness evolves like $h \propto t$, independently of the fluid exponent n. Another system with a similarity solution at $\alpha = 5$ is the axisymmetric viscous GCs flowing over a porous medium (Spannuth *et al.* 2009). Such a similarity among a broad range of physical systems may not be coincidental and could imply a more general symmetry associated with the circular geometry.

Many aspects of the theory were found consistent with experiments performed for the dimensionless parameters $\mathscr{D} \approx 0.15$, $\mathscr{Q} < 0.06$, $1 \ll \mathscr{M} < \mathscr{M}_c$, $\alpha = 1$ and $n > 1$ (Kumar *et al.* 2021). In particular, the time evolution of both fluid fronts predicted by the theory is generally consistent with the power law measured in the experiments. The late-time exponents of r_N in some experiments appear to decline slightly compared to the numerical prediction, though it may be that the experimental data have not fully converged to a late-time solution. In addition, the thickness distribution that we predict for the top fluid layer is in good agreement with the experimental measurements. However, some discrepancies that arise may imply that the theory is not entirely complete. Specifically, the theoretical predictions for the intercepts do not accurately capture the measured ones, particularly in the case of the lubricating front, which evolves faster

than the theoretical predictions. Several potential physical mechanisms that the present theory does not account for may explain these discrepancies. One possible mechanism is that the lubrication front r_L advances as a hydrofracture in between the substrate and the relatively solid viscous fluid layer (Ball & Neufeld 2018), or as a shock in the fluid–fluid interface at r_L (Dauck *et al.* 2019). In addition, the non-uniform colouring of the lower fluid layer (figure 1), which indicates that the thickness of the lower fluid layer is non-monotonic, may reflect a yield stress property of the top fluid layer or an instability of the fluid–fluid interface (Kumar *et al.* 2021). Furthermore, discrepancy between the experimental measurements of r_N before introducing the lubrication fluid $(t/t_L < 1)$ and the theoretical prediction of a non-lubricated GC, particularly for the 2 % polymer concentration (Kumar *et al.* 2021), may imply that the power-law constitutive equation that we use is incomplete. Specifically, the time for the viscosity to adjust to the evolving strain rates may be not instantaneous as we assume, but finite. In addition, polymer entanglements may arise in higher polymer concentrations that potentially drive wall slip at the fluid–solid interface through adhesive failure of the polymer chains at the solid surface or through cohesive failure owing to disentanglement of chains in the bulk from chains adsorbed at the wall (Brochard & De Gennes 1992). The implications of these potential physical mechanisms will be addressed in future studies.

The validity of our assumption that the flow is shear-dominated depends on both the thickness-to-length aspect ratio $\epsilon \equiv \mathcal{H}/\mathcal{R}$ and the boundary conditions at each fluid layer. Under the lubrication assumption $\epsilon \ll 1$, radial forces due to extensional stresses are order ϵ^2 smaller than those due to shear stresses. This is certainly the case for the fluid in the non-lubricated region and for the lubricating fluid in the lubricated region, where the no-slip conditions along the substrate lead to shear-dominated flows. In comparison, the upper fluid layer in the lubricated region experiences less traction along its base due to the lubricating layer beneath, which may imply that extensional stresses can become dominant. Evaluating the extensional radial force in the top layer using our solutions, we find that upstream from the lubricating front, it is indeed much smaller than the radial force due to shear stress. This balance is maintained by a significant back pressure from the non-lubricated region downstream that is dominated by shear (see also Kowal & Worster 2015). The extensional force becomes significant near the singular fluid fronts, where the lubrication approximation does not hold. The flow in the vicinity of the fronts is not parallel to leading order and should, in principle, be modelled as full Stokes flow (Huppert 1982). Nevertheless, independently of the flow details near the fronts, the impact of the fronts on the main flow is not substantial due to the low Reynolds and high Bond numbers (Huppert 1982). This argument is also supported by the consistency that we demonstrate between the predicted shape of the main flow with the experimental measurements (figure 15). Consequently, we believe that for the flow configuration that we consider, the lubrication approximation consistently captures the leading-order dynamics.

Front outstripping may have significant implications on the dominant dynamics, since the elimination of the non-lubricated outer region when $r_N < r_L$ could lead to the dominance of extensional forces, particularly when $\mathcal{M} \gg 1$ (e.g. Fowler & Larson 1978; Bueler & Brown 2009; Mantelli, Haseloff & Schoof 2019). Our present exploration of the route to outstripping always considers the presence of a downstream non-lubricating layer, which keeps our assumption of dominating shear stresses consistent. Exploring the aftermath of outstripping would require extending the present model to account for extensional stresses.

9. Conclusions

Lubricated gravity currents (GCs) are controlled by complex interactions between two fluid layers. The lower, lubricating layer modifies the friction between the substrate and the top layer, which in turn applies stresses that affect the distribution of the lubricating layer. The resulting flow can vary dramatically from other axisymmetric GCs. Specifically, we find that the structure imposed by the upper, non-Newtonian flow precludes self-similarity in general, in contrast with purely Newtonian GCs of a single fluid layer (Huppert 1982) or two coupled layers (Kowal & Worster 2015), and with GCs of shear-thinning power-law fluids (Sayag & Worster 2013).

In spite of the absence of a general global similarity solution, we find a number of asymptotic limits in which similarity solutions do exist. These include the purely Newtonian limit for any mass discharge exponent α, and the case of $\alpha = 5$ for a general power-law fluid. We also find several situations that admit similarity solutions in part of the domain. These include the asymptotic limits of the viscosity ratio, corresponding to the top layer 'solid' ($\mathcal{M} \gg 1$) and 'liquid' ($\mathcal{M} \ll 1$) limits, and the solution in the vicinity of the fluid fronts.

Among the important consequences of the absence of global similarity is the potential for front outstripping, in which the lubricating fluid front outstrips the outer fluid front. Outstripping can emerge through two mechanisms. Exponent outstripping occurs when $(\alpha - 5)(n - 1) > 0$, which arises due to the difference in the exponents that determine the late-time evolution of the fluid fronts. This implies front outstripping for either shear-thinning or shear-thickening top fluids, depending on the discharge exponent α. Intercept outstripping emerges above a critical viscosity ratio $\mathcal{M}_c(\mathcal{Q}, \mathcal{D}, \alpha, n)$, regardless of the fronts' time-evolution exponents. In particular, such outstripping can emerge also in a regime of global self-similarity, such as when $n = 1$ or $\alpha = 5$.

In the canonical case of constant flux ($\alpha = 1$), our solutions are found consistent with laboratory experiments (Kumar *et al.* 2021) in predicting both the time exponents of the front evolution and the thickness fields. Discrepancies in the front intercepts, particularly that of the lubricating fluid front, suggest that additional physical mechanisms may contribute to the front evolution, such as hydrofracturing or wall-slip along the substrate, and potentially extensional stresses in the top layer that may become significant at the approach to front outstripping. Exploration of these mechanisms will be the topic of future studies.

As far as we know, axisymmetric patterns of lubricated GCs have not been observed in natural settings, such as ice sheets. Nevertheless, experimental evidence suggest that such patterns can exist in some regime of parameters (Kumar *et al.* 2021). Therefore, supported by this evidence, our analysis may point to the potential existence of axisymmetric patterns in the natural setting. We note that the same experimental set-up also shows evidence for non-axisymmetric patterns under some conditions, which may be more common in the natural setting, such as ice sheets, in the form of ice streams and surges. We intend to explore those in future studies.

Declaration of interests. The authors report no conflict of interest.

Author ORCIDs.
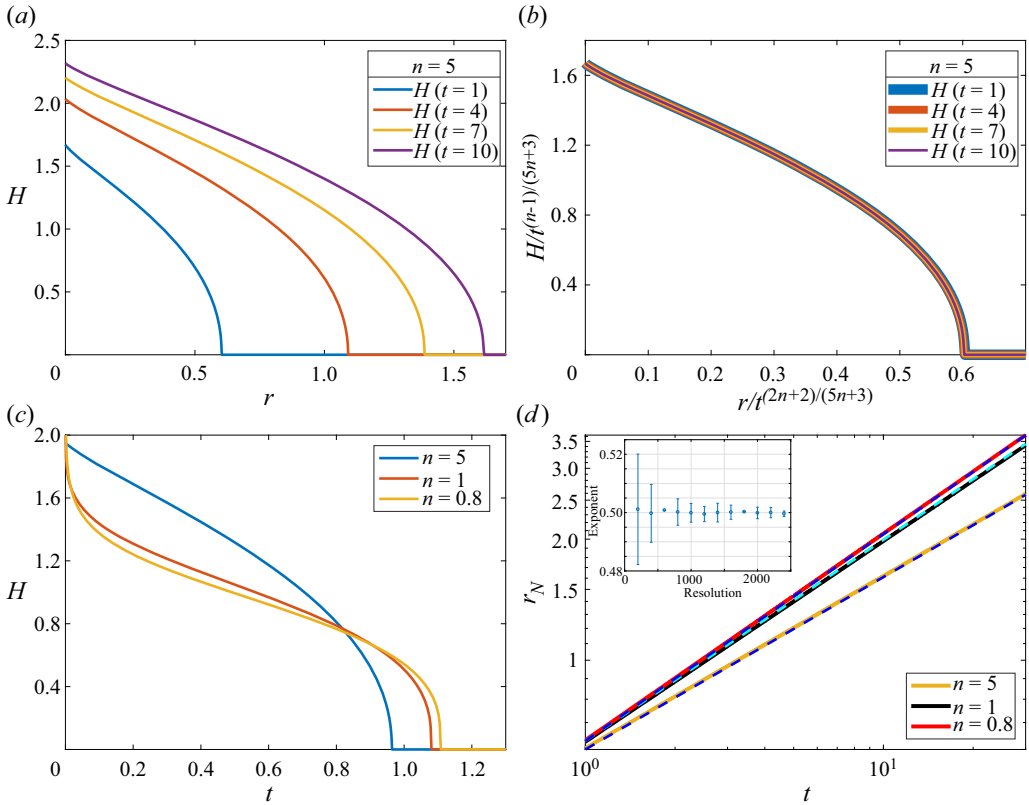Ⓑ Roiy Sayag https://orcid.org/0000-0002-1672-982X.

Figure 16. Validation of the lubricated GC numerical solution with the theoretical prediction of non-lubricated GC of power-law fluids ($\mathcal{Q} = 0$, $\alpha = 1$; Sayag & Worster 2013). Fluid height for $n = 5$ at non-dimensional times $t = 1, 4, 7, 10$ in (*a*) the regular thickness–radius space, and (*b*) the thickness–radius space normalized by the theoretical prediction. (*c*) Fluid height for $n = 5$, 1 and 0.8, at non-dimensional time $t = 3$. (*d*) The front $r_N(t)$ (solid), and the theoretical prediction for $n = 5$, 1 and 0.8 (dashed). The inset shows regression results to the slope (exponent) of the numerical solution for $n = 1$ as a function of spatial resolution in the range 200–2400 points in logarithmic spaced mesh. Error bars represent the root-mean-square deviation of the fitted curve to the fronts.

Appendix A. Validation of the numerical code

A.1. *Non-lubricated gravity currents*

The model that we develop in §2 describes in the limit $\mathcal{Q} = 0$ a non-lubricated GC that propagates under a no-slip condition along the substrate. Such a flow is similar to the flow in the non-lubricated region, and is known to have a similarity solution (Sayag & Worster 2013)

$$h(r, t) \propto t^{(n-1)/(5n+3)}, \quad r_N(t) \propto t^{(2n+2)/(5n+3)}, \tag{A1a,b}$$

for constant flux $\alpha = 1$. We use this solution to validate our numerical solution in the $\mathcal{Q} = 0$ limit. Specifically, we solve the dimensionless equation set (§2.3) with $\mathcal{Q} = 0$, zero initial thickness $H(r, 0) = 0$, and logarithmically spaced spatial mesh with 1200 points. We find our solutions for the fluid height and for the leading front consistent with the theoretical predictions (figure 16). Repeating the same computation for varying spatial resolutions, we find that the convergence accuracy of the front exponent to the predicted theoretical value grows with the number of spatial grid points (figure 16*d*, inset).
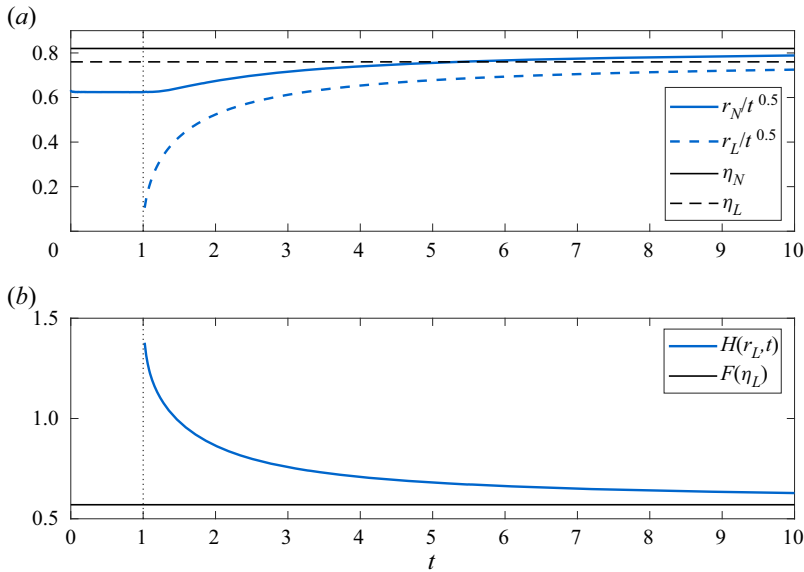
Figure 17. Validation of the lubricated GC numerical solution with the Newtonian ($n = 1$) lubricated GC (blue) with $\mathcal{M} = 10\,000$, $\mathcal{Q} = 0.2$ and $\mathcal{D} = 0.1$, showing the convergence of the normalized fronts (*a*) and the lubricated fluid height at lubricating fluid front, r_L (*b*) to the theoretically predicted constant values (black).

A.2. *Newtonian lubricated gravity currents*

In the limit $n = 1$, $\alpha = 1$, our numerical model converges to the purely Newtonian lubricated GC discharged at constant flux (Kowal & Worster 2015). Considering first the specific case where $\mathcal{M} = 10\,000$, $\mathcal{Q} = 0.2$ and $\mathcal{D} = 0.1$, we find that both the fronts r_N, r_L and the upper fluid height at the lubricant front $H(r_L)$ converge to the theoretical values η_N, η_L and $F(\eta)$, respectively (figure 17). Second, we find that our solutions for the coefficients η_N and η_L are consistent with the theoretical predictions for a wide range of $\mathcal{M}$ values (figure 11). As shown in § A.1, small discrepancies from the predicted values are due to low spatial resolution. Finally, the solutions to the specific regime discussed in § 6 (figure 9) is more evidence for the consistency between our numerical results and those of Kowal & Worster (2015, figure 13).

REFERENCES

BALL, T.V. & NEUFELD, J.A. 2018 Static and dynamic fluid-driven fracturing of adhered elastica. *Phys. Rev. F* **3** (7), 074101.

BALMFORTH, N.J., BURBIDGE, A.S., CRASTER, R.V., SALZIG, J. & SHEN, A. 2000 Visco-plastic models of isothermal lava domes. *J. Fluid Mech.* **403**, 37–65.

BROCHARD, F. & DE GENNES, P.G. 1992 Shear-dependent slippage at a polymer/solid interface. *Langmuir* **8** (12), 3033–3037.

BUELER, E. & BROWN, J. 2009 Shallow shelf approximation as a 'sliding law' in a thermomechanically coupled ice sheet model. *J. Geophys. Res.* **114** (F3), F03008.

CREYTS, T.T. & SCHOOF, C.G. 2009 Drainage through subglacial water sheets. *J. Geophys. Res.* **114** (F4), F04008.

DANIEL, D., TIMONEN, J.V.I., LI, R., VELLING, S.J. & AIZENBERG, J. 2017 Oleoplaning droplets on lubricated surfaces. *Nat. Phys.* **13** (10), 1020–1025.

DAUCK, T.F., BOX, F., GELL, L., NEUFELD, J.A. & LISTER, J.R. 2019 Shock formation in two-layer equal-density viscous gravity currents. *J. Fluid Mech.* **863**, 730–756.

DECONTO, R.M. & POLLARD, D. 2016 Contribution of Antarctica to past and future sea-level rise. *Nature* **531** (7596), 591–597.

FOWLER, A.C. 1981 A theoretical treatment of the sliding of glaciers in the absence of cavitation. *Phil. Trans. R. Soc. Lond.* A **298** (1445), 637–681.

FOWLER, A.C. 1987 A theory of glacier surges. *J. Geophys. Res.* **92** (B9), 9111–9120.

FOWLER, A.C. & JOHNSON, C. 1995 Hydraulic run-away – a mechanism for thermally regulated surges of ice sheets. *J. Glaciol.* **41** (139), 554–561.

FOWLER, A.C. & LARSON, D.A. 1978 On the flow of polythermal glaciers – I. Model and preliminary analysis. *Proc. R. Soc. Lond.* A **363** (1713), 217–242.

GLEN, J.W. 1952 Experiments on the deformation of ice. *J. Glaciol.* **2** (12), 111–114.

GRIFFITHS, R.W. 2000 The dynamics of lava flows. *Annu. Rev. Fluid Mech.* **32**, 477–518.

HUPPERT, H.E. 1982 The propagation of two-dimensional and axisymmetric viscous gravity currents over a rigid horizontal surface. *J. Fluid Mech.* **121**, 43–58.

IVERSON, N.R., HOOYER, T.S. & BAKER, R.W. 1998 Ring-shear studies of till deformation: Coulomb-plastic behavior and distributed strain in glacier beds. *J. Glaciol.* **44** (148), 634–642.

JOUGHIN, I., MACAYEAL, D.R. & TULACZYK, S. 2004 Basal shear stress of the Ross ice streams from control method inversions. *J. Geophys. Res.* **109** (B9), B09405.

KAMB, S.B. 2001 Basal zone of the west Antarctic ice streams and its role in lubrication of their rapid motion. In *The West Antarctic Ice Sheet – Behaviour and Environment* (ed. R.B. Alley & R.A. Bindschadler), Antarctic Research Series, vol. 77. AGU.

KASMALKAR, I., MANTELLI, E. & SUCKALE, J. 2019 Spatial heterogeneity in subglacial drainage driven by till erosion. *Proc. R. Soc. Lond.* A **475** (2228), 20190259.

KEISER, A., KEISER, L., CLANET, C. & QUÉRÉ, D. 2017 Drop friction on liquid-infused materials. *Soft Matt.* **13** (39), 6981–6987.

KIVELSON, M.G., KHURANA, K.K., RUSSELL, C.T., VOLWERK, M., WALKER, R.J. & ZIMMER, C. 2000 Galileo magnetometer measurements: a stronger case for a subsurface ocean at Europa. *Science* **289** (5483), 1340–1343.

KOWAL, K.N. & WORSTER, M.G. 2015 Lubricated viscous gravity currents. *J. Fluid Mech.* **766**, 626–655.

KOWAL, K.N. & WORSTER, M.G. 2019*a* Stability of lubricated viscous gravity currents. Part 1. Internal and frontal analyses and stabilisation by horizontal shear. *J. Fluid Mech.* **871**, 970–1006.

KOWAL, K.N. & WORSTER, M.G. 2019*b* Stability of lubricated viscous gravity currents. Part 2. Global analysis and stabilisation by buoyancy forces. *J. Fluid Mech.* **871**, 1007–1027.

KUMAR, P., ZURI, S., KOGAN, D., GOTTLIEB, M. & SAYAG, R. 2021 Lubricated gravity currents of power-law fluids. *J. Fluid Mech.* **916**, A33.

KYRKE-SMITH, T.M. & FOWLER, A.C. 2014 Subglacial swamps. *Proc. R. Soc. Lond.* A **470** (2171), 20140340.

KYRKE-SMITH, T.M., KATZ, R.F. & FOWLER, A.C. 2013 Subglacial hydrology and the formation of ice streams. *Proc. R. Soc. Lond.* A **470**, 30494.

LISTER, J.R. & KERR, R.C. 1989 The propagation of two-dimensional and axisymmetric viscous gravity currents at a fluid interface. *J. Fluid Mech.* **203**, 215–249.

MANTELLI, E., HASELOFF, M. & SCHOOF, C. 2019 Ice sheet flow with thermally activated sliding. Part 1: the role of advection. *Proc. R. Soc. Lond.* A **475** (2230), 20190410.

NANNI, U., GIMBERT, F., ROUX, P. & LECOINTRE, A. 2021 Observing the subglacial hydrology network and its dynamics with a dense seismic array. *Proc. Natl Acad. Sci. USA* **118** (28), e2023757118.

PEGLER, S.S. & WORSTER, M.G. 2012 Dynamics of a viscous layer flowing radially over an inviscid ocean. *J. Fluid Mech.* **696** (-1), 152–174.

SAYAG, R. & TZIPERMAN, E. 2009 Spatiotemporal dynamics of ice streams due to a triple-valued sliding law. *J. Fluid Mech.* **640**, 483–505.

SAYAG, R. & WORSTER, M.G. 2013 Axisymmetric gravity currents of power-law fluids over a rigid horizontal surface. *J. Fluid Mech.* **716**, R5.

SAYAG, R. & WORSTER, M.G. 2019 Instability of radially spreading extensional flows. Part 1. Experimental analysis. *J. Fluid Mech.* **881**, 722–738.

SCHOOF, C. 2004 On the mechanics of ice-stream shear margins. *J. Glaciol.* **50** (169), 208–218.

SCHOOF, C. & HEWITT, I. 2013 Ice-sheet dynamics. *Annu. Rev. Fluid Mech.* **45** (1), 217–239.

SPANNUTH, M.J., NEUFELD, J.A., WETTLAUFER, J.S. & WORSTER, M.G. 2009 Axisymmetric viscous gravity currents flowing over a porous medium. *J. Fluid Mech.* **622**, 135–144.

STOKES, C.R., CLARK, C.D., LIAN, O.B. & TULACZYK, S. 2007 Ice stream sticky spots: a review of their identification and influence beneath contemporary and palaeo-ice streams. *Earth Sci. Rev.* **81** (3–4), 217–249.

Tulaczyk, S., Kamb, W.B. & Engelhardt, H.F. 2000 Basal mechanics of ice stream B, West Antarctica 1. Till mechanics. *J. Geophys. Res.* **105** (B1), 463–481.

Vogel, S.W., Tulaczyk, S., Kamb, B., Engelhardt, H., Carsey, F.D., Behar, A.E., Lane, A.L. & Joughin, I. 2005 Subglacial conditions during and after stoppage of an Antarctic ice stream: is reactivation imminent? *Geophys. Res. Lett.* **32** (14), L14502.

Walder, J.S. 1982 Stability of sheet flow of water beneath temperate glaciers and implications for glacier surging. *J. Glaciol.* **28** (99), 273–293.

Woods, A.W. & Mason, R. 2000 The dynamics of two-layer gravity-driven flows in permeable rock. *J. Fluid Mech.* **421**, 83–114.